2022-12-01

Pioneering Concepts For 3D Electromagnetics

Cesar Valle
University of Texas at El Paso

PIONEERING CONCEPTS FOR 3D ELECTROMAGNETICS

CESAR LUIS VALLE

Doctoral Program in Electrical and Computer Engineering

APPROVED:

Raymond C. Rumpf, Ph.D., Chair

David Zubia, Ph.D.

Joel Quintana, Ph.D.

Robert Roberts, Ph.D.

Stephen L. Crites, Jr., Ph.D.
Dean of the Graduate School

Dedication

To my loving family for their infinite patience.

PIONEERING CONCEPTS FOR 3D ELECTROMAGNETICS

by

CESAR LUIS VALLE

DISSERTATION

Presented to the Faculty of the Graduate School of

The University of Texas at El Paso

in Partial Fulfillment

of the Requirements

for the Degree of

DOCTOR OF PHILOSOPHY

Department of Electrical and Computer Engineering

THE UNIVERSITY OF TEXAS AT EL PASO

December 2022

Acknowledgements

To all my friends and family for their continued support on my journey for higher education. To my friend and advisor, Dr. Raymond C. Rumpf, the world's greatest electromancer who has taught me everything I know. My labmates Gilbert, Sarah, Manny, Edgar, Noel, Ubaldo, Jesus and Galib for all the good meals and laughs along the way. Thank you all for making these difficult PhD years fun.

Abstract

This work introduces two paradigm changing concepts that will push electromagnetics (EM) to the third dimension. The first of that work involves the introduction of the conformal Spatially Variant Lattice (SVL) algorithm that can conform any periodic structure onto arbitrary curvature. The algorithms robustness is confirmed by conforming a frequency selective surface (FSS) onto an extreme paraboloid, proving the algorithms robustness on high sloping surfaces. Three FSSs were made in total; a standard flat FSS, a projected FSS, and a FSS made through the conformal SVL algorithm. Measured results are shown and match well to simulation.

Secondly, in the world of 3D printing, a lot of research focuses on printing devices that are already manufactured much better by other means. Producing designs that fully exploit the third dimension is desperately needed in order to truly showcase the potential of 3D printing. Initial steps were proven via the production of the world's first true 3D/volumetric circuit and the early design of 3D radio frequency (RF) interconnects. In this work, design rules and best practices for hybrid printing of arbitrary metal/dielectric structures are pioneered through the manufacturing of a volumetric compact ultrawideband antenna (CUA). The antenna's manufacturing was explored in three different ways. First a design was printed in plastic and then coated in conductive paste, emulating the electroplating approach typically found in literature. Second, a 2.5D segment stacking approach was explored by hybrid printing the CUA in multiple segments. Lastly, a CUA was printed as a true hybrid print in a monolithic design using a single print job. Electromagnetic measurements of the voltage standing wave ratio (VSWR) between these three approaches are compared.

Through the combination of algorithms and hybrid printing uniquely tailored for 3D, EM design can take advantage of what can be offered by the third dimension. Circuits can be radically

miniaturized and made to fit unconventional form factors, conformal printing algorithms can be explored, 3D/volumetric antenna designs and metamaterial based approaches among many more can be explored.

Table of Contents

List of Tables

List of Figures

Chapter 1: Introduction

1.1 Review of 3D Printing Technologies and History

Fused deposition modeling (FDM) is the process that is typically thought of when 3D printing is mentioned. The process itself was invented by Scott Crump, co-founder of Stratasys. The technology was patented and commercialized by Stratasys who holds many early intellectual property on the process [1-4]. As an additive process, it consists of depositing thin layers of material onto a heated bed. Material is continuously fed into a heated nozzle for melting at predetermined temperatures that depend on the material that is being deposited. The most popular materials being acrylonitrile butadiene styrene (ABS) and polylactic acid (PLA). Upon the expiration of Stratasys' final patent the technology began to be developed further leading to novel ideas and implementations. To further expand the versatility of FDM, different types of materials have been investigated. One example is a highly conductive filament that has been used to 3D print metamaterials by Duke University, although ultimately not feasible for printing conducting paths [5]. That task alone has been primarily left to silver ink. Other forms of depositing ink through aerosol sprays has been investigated and commercialized by Optomec leading to new copper based conductive inks [6]. The combination of FDM printed substrates and dispensed conductive inks has led to an interest in printing fully functional radio frequency (RF) devices in one process. Of note is a 2.4 GHz Bluetooth/Wi-Fi antenna printed using nScrypt trademarked technology [7, 8]. Further developments in this area of 3D printing involve conforming prints onto surfaces [9, 10]. For the development of circuits and RF devices, the combination of FDM along with conductive ink dispensing (hybrid manufacturing) is preferred.

Another popular method of manufacturing is stereolithography. The process itself is attributed to Charles W. Hull who patented the technology in 1984 [11]. As opposed to building

models by depositing plastic layers, stereolithography makes use of ultraviolet light to cure photosensitive resins. Designs are still printed on a layer by layer basis. In a similar fashion, it is common to see a combination of stereolithography and dispensing to form functional circuits. A plastic substrate with paths for conductive leads in combination with ink dispensing was used to achieve a functional 555 timer circuit [12]. This type of process has been radically miniaturized and has been shown to be able to print "micro-optical" structures using what is called multi-photon three-dimensional microfabrication (3DM) [13]. A photonic crystal lattice capable of bending a beam of light at a 90° bend was implemented in a 64,000 μm3 volume using 3DM [14].

Many more forms of additive manufacturing remain popular and continue to be modified/customized. Selective laser sintering (SLS) is another popular form of additive manufacturing used today. Originally patented by Carl R. Deckard and funded by DARPA in 1986, this process builds 3D structures by sintering a laser on a bed of metal powder [15]. General Electric (GE) has plans of developing a large volume SLS machine through their new branch GE Additive [16, 17]. A similar technology is also currently under test by NASA's Marshall Space Flight Center to build rocket parts [18]. The various forms of 3D printing have been modified and extended to countless new/hybridized methods further proving the versatility of 3D printing. New methods will continue to be developed to suit the needs of different professional fields.

1.2 Review of 3D Printed Circuits and EM Devices

3D printing has evolved to the point of being capable of producing finished devices [19]. In the field of electromagnetic devices and circuits, this is often done by multimaterial processing combining the use of a dielectric insulator and some type of conductive ink/paste or copper wiring. The specific processes and technologies that are combined often varies. A popular combination is that of the stereolithography (SLA) for dielectrics and aerosol inkjet technologies for conductors.

A combination of silver nanoparticle ink tracings embedded in a photocurable polymer that connect a light emitting diode (LED) to a power source has been achieved [20]. A novel aspect of this research is the ability to improve the conductivity of silver ink through laser sintering of conductive traces as well as the multi-layer embedding of the silver ink itself within the dielectric layers. Other efforts were capable of conforming inkjet technology to a variety of structures from a cube to a two-chamber water tank with fluid level sensors [10]. The University of South Florida in collaboration with W.M. Keck Center at the University of Texas at El Paso (UTEP) has combined the SLA process and the microdispensing of silver conductive inks to produce a half-wave dipole conformed to the surface of a cube that is capable of operating at 2.45 GHz [21]. The fabrication of functional devices is not limited to the combination of SLA and dispensing. FDM printed plastic substrates and microdispensing of conductive inks is often combined as well. A phased array antenna unit cell front end complete with the integration of a filter, chip balun, and phase shifter has been achieved [22, 23]. This work combines discrete circuit components along with FDM and microdispensing to create a finished product. Other efforts do not use conductive inks at all. Instead, two FDM dispensing heads are used to combine plastic filaments and conductive copper based filaments to print passive devices such as capacitors, inductors, and resistors [24, 25]. Another unique effort combines FDM with copper wire embedding as a way of avoiding the use of silver ink due to its lower conductivity when compared to copper [26]. This work makes use of FDM printed plastic substrates and copper-wire cutting head for conductive traces.

Many other works exist that combine the plethora of 3D printing processes to create finished products. This goes to show that the technology to generate these types of products exists and continues to be investigated. What remains to be developed are the design processes and best

practices for these types of technologies. On top of this, there is also a need for an all-encompassing software package that is capable of handling hybrid 3D printing processes. An example of this is an effort by W.M. Keck Center at UTEP that creates a software package that combines FDM along with their wire embedding technology [27]. This package takes an electrical design schematic along with a computer-aided design (CAD) model and combines them in order to generate the code necessary to print the design. This is all done within the same user-interface thus eliminating the need to use multiple programs to generate the files necessary to drive 3D printers. Our vision of 3D circuits is not exempted from this need and the development of design practices.

Recently, the world's first truly three-dimensional circuit has been accomplished [28]. In a true three-dimensional or volumetric circuit components are arbitrarily placed in position and orientation. Conductive paths follow spline-like curves throughout the volume. Even the overall geometry the circuit is embedded in can be arbitrary. In order to be able to manufacture a 3D design such as this, a major advancement in 3D printing slicing software had to first be achieved [29]. Current software only allows for the printing of flat conventional designs. Devices are typically completed in at minimum a two-step process. First plastic substrate pieces are printed with a process such as fused deposition modeling (FDM). Once these pieces are done, a conductive layer is added to the top of the substrate (ex. microdispensing). Through the use of modern slicers like the one referenced, devices can now be printed in a single step process capable of alternating between plastic and conductive layers throughout the entire printing process. A combination of hybrid slicing and a new 3D design paradigm is set to revolutionize conventional electromagnetic design.

1.3 MOTIVATION

Despite the versatility afforded though hybrid 3D printing and modern slicers, the majority of electromagnetic design remains stuck in the second dimension. 3D designs and fabrication processes have seldom been investigated. In literature, for circuit design we see approaches that could be described as 2.5D at best. The approach taken is similar to stacking printed circuit board (PCB) on top of each other and connecting them vertically with the use of vias [30, 31]. In a true 3D/volumetric circuit components can be placed in any position throughout all three dimensions as well as in any orientation. Interconnects can meander smoothly throughout the volume following spline-like paths. 3D circuit designs in general are expected to have many benefits over their conventional "flat" or 2D counterparts. Some of these benefits are:

- Smaller form factor leading to lighter more compact circuit models by minimizing the overall area needed for a planar design into a volume
- Unconventional form factors that fit to any desired specification
- Arbitrary conformal form factors and designs
- Reduced parasitic impedances due to the use of smooth spline-like interconnects leading to larger bandwidth
- Minimized trace lengths leading to highly efficient circuits

For the last several years, the field of 3D printing has enjoyed significant improvements and advancements in technology. For 3D printing to take the next leap, true 3D designs need to be explored. Designs that are well suited for 3D printing and can take advantage of what the third dimension can offer. The goal of this dissertation is to pioneer 3D/volumetric EM concepts. The approach was twofold. First, an algorithm that generates a frequency selective surface (FSS) design onto arbitrary curvature will be developed, applied, and verified through electromagnetic

measurements. Second hybrid 3D printing design rules and best practices will be explored through the hybrid 3D printing of a compact ultrawideband antenna (CUA) design. The generated design rules and best practices can be applied to virtually any 3D metal/dielectric structure.

1.4 OUTLINE

Chapter 2 begins by introducing the conformal SVL algorithm. This algorithm is capable of optimizing the layout of a periodic structure for operation on virtually any curved surface. All while maintaining the overall size, shape, and spacing of the periodic elements. The periodicity is maintained no matter how abrupt the curvature is. The algorithm is agnostic to both unit cell and element type.

Chapter 3 introduces hybrid printing enabled by the use of commercial software OmniSlice™. Two examples of 3D printed wearable electronics are presented. This is followed by the world's first 3D circuit and 3D RF interconnects. Printing parameters and initial best practices are introduced.

Chapter 4 applies the conformal SVL algorithm to a Jerusalem cross (JC) element by conforming it onto a doubly curved surface. The algorithm was tested with the use of an abrupt, highly sloping curvature. The response of the conformal array was compared to a flat array and a projected array. EM measured results were found to be in agreement with simulation.

Chapter 5 explores the hybrid 3D printing of a volumetric ultrawideband antenna design. The printing parameters, design rules, and best practices introduced in Chapter 3 are further polished to yield a functional 3D/volumetric antenna. The design rules developed here can be applied to virtually any arrangement of metal/dielectric structures.

Lastly, this work is concluded in Chapter 6 with a summary of core contributions and suggestions for future work.

Chapter 2: Algorithm for Conforming Periodic Structures onto Arbitrary Curvature

2.1 Background

A frequency selective surface (FSS) is a periodic array of identical elements designed to either stop or pass certain frequencies in a given range [32]. They can also be simply thought of as flat electromagnetic filters. The properties of a FSS can be uniquely tailored via element design. Common element designs range from loop elements [33]-[36], to square, circular or hexagonal plates [37]-[40], fractal designs [41]-[43], and even "3D" element designs [44], [45]. Slotted arrays are another popular form of design and feature band pass behavior [46], [47]. Not limited to metallic elements, FSS designs can be all dielectric based on guided-mode resonance (GMR) and prove particularly useful for high-power applications [48]-[50]. Other popular forms of design are current sheet arrays or active arrays [51]-[53]. The wide variety of element designs and form of operation (active, passive, reflective, etc.) give the user a seemingly limitless choice when it comes to array design.

In application, an infinitely flat periodic array illuminated by a plane-wave is ideal but non-existent. Practical use of FSS designs usually require a finite flat design to be fitted on some curvature. These applications include radar cross section (RCS) reduction on antenna radomes [54], RCS reduction designs on planes for stealth applications [55]-[57], and electromagnetic shielding [38],[45] among many more. Recently, with advances in additive manufacturing, there has been interest in placing FSS designs onto bendable or flexible 3D printed substrates [58], [59]. 3D printing systems that make use of more than three axes are also a good fit for manufacturing conformal electronics and FSSs [60], although the EM Lab has recently demonstrated it is possible to print conformally onto near-vertical sidewalls using ordinary three-axis printers [96].

Despite a plethora of element designs and applications, very little work has been done regarding the effects of placing periodic structures on arbitrary curved surfaces. Very often, FSS arrays are designed without thought to the curvature they will be placed on. Common practice is to design a flat array and project it onto whatever curvature the application requires. This can deform the elements that lie on slopes ([61]-[63]) and often destroys periodicity making the array non-functional. In other examples, FSSs are conformed to canonical shapes or surfaces with a large bend radius [64], [65]. Examples of compensating for curvature include a 1D GMR filter where the period was chirped to compensate for the curved surface it was placed on as well as the curvature of the spherical wave front illuminating the device [48]. Similar extensions of this method can be found for 2D conformal array analysis that take a more careful consideration how elements are placed and rotated along a curve [66], [67]. However, a tool that is capable of placing any array of elements onto any form of curvature without distorting its properties is needed. In previous work, an algorithm was developed that can spatially vary or functionally grade different aspects of a periodic lattice while keeping the lattice smooth, continuous, and defect free. This spatially-variant lattice (SVL) algorithm was used to generate abrupt photonic crystal bends [68], generate spatially-variant anisotropic metamaterials [69], form novel lenses into photonic crystals [70], and metamaterial devices designed by transformation optics [71]. Not limited to photonic crystals, the SVL algorithm can be applied to any periodic structure including reflectarrays [72]-[73], phased array antennas [36],[51],[52], metasurfaces [74]-[75], and more. This chapter introduces the conformal SVL algorithm capable of optimizing the layout of a FSS for operation on virtually any curved surface while maintaining the overall size, shape, and spacing of the FSS elements. In comparison to popular projection techniques, the conformal SVL algorithm preserves the geometry of the array no matter how abrupt or highly sloping the curvature is. The conformal

SVL algorithm is also agnostic to both the curvature and element type. The algorithm is best described as a geometry tool capable of preserving the overall size, shape, and spacing between elements. Other techniques capable of distributing elements over geometries exist, but are rare and are extremely limited in their ability to maintain consistent size, shape and spacing of the elements. One such technique, UV unwrapping, is commonly used in artistic rendering tools to apply 2D textures onto 3D objects [97, 98]. A 3D object is "unwrapped" by placing seams or cuts in the model to unfold it onto an equivalent 2D surface. For the application of conformal FSSs, elements can be projected onto the 2D surface after which the surface can be folded back into its original 3D shape. However, the introduction of seams or cuts creates discontinuities on the surface. The more complex a 3D surface the more seams it must contain where periodicity will not be enforced, thus degrading the EM performance. Another popular technique for distributing elements on surfaces or objects is done via the use of the Poisson disk random distribution [99]. However, as the name implies, the distribution of elements across a surface is done randomly. By its very nature periodicity is not enforced often leading to elements that are too close in spacing in some areas and large gaps in others [100]. In contrast, the conformal SVL tool is capable of maintaining an even spacing between elements over the entire surface regardless of the shape of the surface.

2.2 Defining Grating Vector Across Arbitrary Curvature

The approach for arranging periodic elements begins with the generation of SVL gratings as outlined in [68]. The SVL algorithm is well covered in literature therefore only the modifications made to it that are relevant for this research are described. In a form that is analogous to a wave vector, a grating vector $\vec{K}(\vec{r})$ is defined as a function of position $\vec{r}$ as

$$\vec{K}(\vec{r}) = \frac{2\pi}{\Lambda(\vec{r})}\left\{\hat{x}\cos\left[\theta(\vec{r})\right] + \hat{y}\sin\left[\theta(\vec{r})\right]\right\} \tag{2.1}$$

where $\Lambda(\vec{r})$ is the period of the grating and $\theta(\vec{r})$ is the orientation of the grating, both as functions of position with the position vector as $\vec{r} = x\hat{x} + y\hat{y}$. To properly calculate the grating when the grating vector is a function of position, an intermediate parameter called the grating phase $\Phi(\vec{r})$ is introduced. This is related to the grating vector through

$$\nabla\Phi(\vec{r}) = \vec{K}(\vec{r}). \tag{2.2}$$

Equation (2.2) is overdetermined and therefore solved in the sense of least squares. From its solution, a spatially variant grating $\varepsilon(\vec{r})$ is calculated according to

$$\varepsilon(\vec{r}) = \cos\left[\Phi(\vec{r})\right]. \tag{2.3}$$

Up to this point, spatially-variant gratings are generated across a flat plane with no information about the curvature or object the grating will be placed onto. In order to account for curvature, the grating period needs to be modified as a function of position. Figure 2.1 shows a diagram of the cross section of a curve used to adjust the period in a way that accounts for curvature.

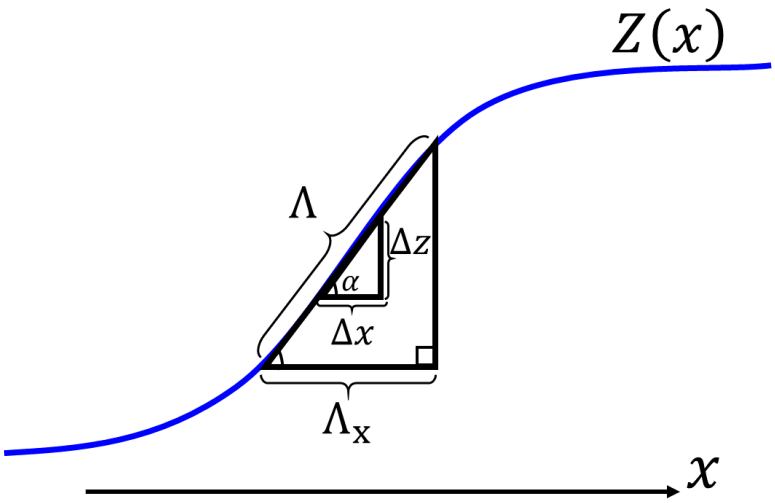

Figure 2.1 Fictitious curved surface $Z(x)$ used to calculate the adjusted period Λ_x.

The curve $Z(x)$ is the surface onto which a periodic structure will be placed. Two similar triangles are defined both containing the angle α. The larger triangle contains the hypotenuse of

length Λ representing the period along the curved surface without any modifications and stretched out by the curvature. The period Λ_x represents the adjusted period that will be used as an input to the SVL algorithm. The smaller triangle shown contains sides Δx and Δz. Using the smaller triangle, an expression for the angle α is found and limit as Δx and Δz approach zero is taken. The result arrives at

$$\alpha = \tan^{-1}\left(\frac{dz}{dx}\right). \tag{2.4}$$

Due to the nature of similar triangles, the angle α also has the relation

$$\cos(\alpha) = \frac{\Lambda_x}{\Lambda} \tag{2.5}$$

based on the larger triangle. By substituting α from (2.4) into (2.5), Λ_x can be derived as

$$\Lambda_x = \Lambda \cos\left[\tan^{-1}\left(\frac{dz}{dx}\right)\right]. \tag{2.6}$$

This is the adjusted input period for curvature along only the x direction. This can be generalized for a 2D surface along the *x* and *y* directions by calculating the gradient of the surface in the direction of the grating vector. This leads to a new adjusted period that is also a function of position

$$\Lambda'(\vec{r}) = \Lambda(\vec{r})\cos\left\{\tan^{-1}\left[\nabla Z(\vec{r})\bullet\frac{\vec{K}(r)}{\left|\vec{K}(r)\right|}\right]\right\} \tag{2.7}$$

where $\Lambda'(\vec{r})$ is the adjusted period in 2D and $Z(\vec{r})$ describes the surface the array will placed onto. Finally, equation (2.1) is modified by substituting (2.7) in place of the original grating period.

$$\vec{K}(\vec{r}) = \frac{2\pi}{\Lambda'(\vec{r})}\left\{\hat{x}\cos\left[\theta(\vec{r})\right] + \hat{y}\sin\left[\theta(\vec{r})\right]\right\} \tag{2.8}$$

2.3 Generating Planar Gratings and Deformation Control

To build an array, two separate planar gratings need to be calculated. These gratings are generated through the use of reciprocal lattice vectors. Different sets of vectors can be used for hexagonal symmetry, rectangular symmetry, etc. For square symmetry the reciprocal lattice vectors are

$$\vec{T}_1 = \frac{2\pi}{\Lambda}\hat{x} \tag{2.9}$$

$$\vec{T}_2 = \frac{2\pi}{\Lambda}\hat{y} \tag{2.10}$$

where the coefficient Λ in both expressions is the period of the FSS. Figure 2.2 shows examples of planar gratings for square symmetry generated over different surfaces. The top row shows gratings generated on a plane with no curvature (standard SVL algorithm output). The middle row shows planar gratings whose period has been adjusted to account for the curvature of a two dimensional Gaussian surface. The bottom row shows the same grating generated over a randomly generated surface. The third column shows the sum of the two planar gratings. The intersections of the two gratings are used to identify the locations of the FSS elements.

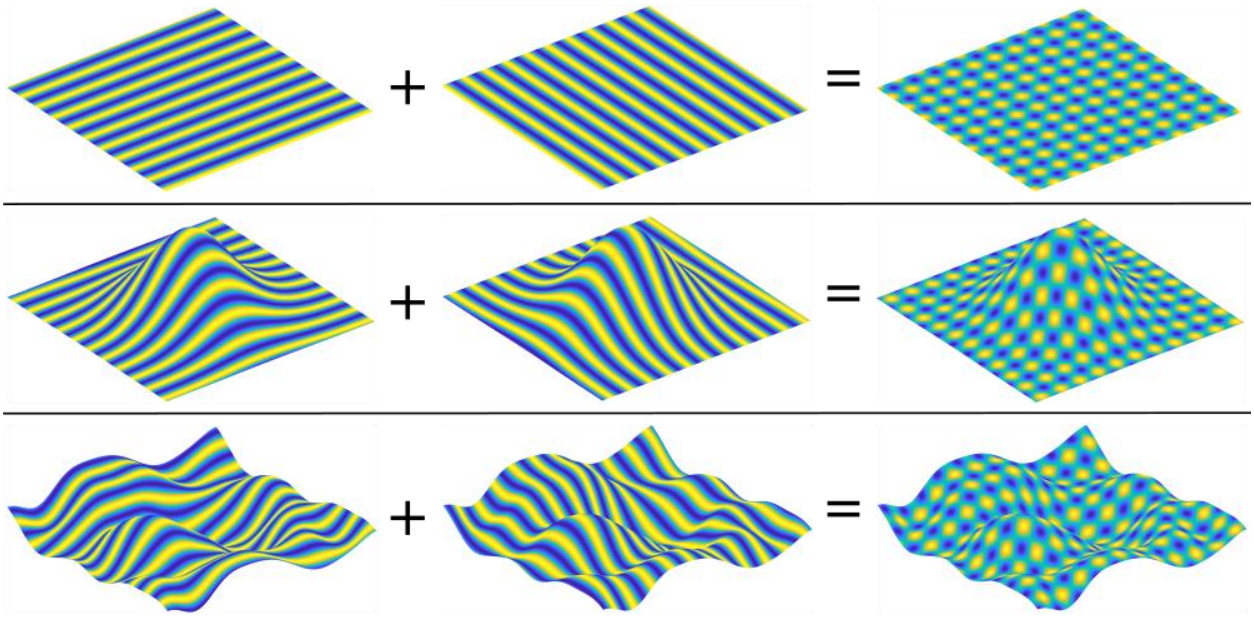

Figure 2.2 The two columns show a plot of planar gratings generated using reciprocal lattice vectors $\vec{T}_1$ and $\vec{T}_2$. The first row shows the combination of the two gratings generated on a flat plane by the SVL algorithm. The second row shows the same two gratings generated across a Gaussian curve. The third row shows the same gratings generated across a random surface.

Due to the algorithm being solved in the sense of least squares (i.e. best fit), some slight deformations in the period and orientation may exist. These deformations can be improved via deformation control described in the appendix of [76]. For the application of FSSs, it was decided to reinforce the period of the device at the expense of orientation. This is acceptable especially when elements are chosen that are polarization independent due to having rotational symmetry. Although a subtle change, Figure 2.3 shows the comparison between a lattice with no deformation control and one with a reinforced period.

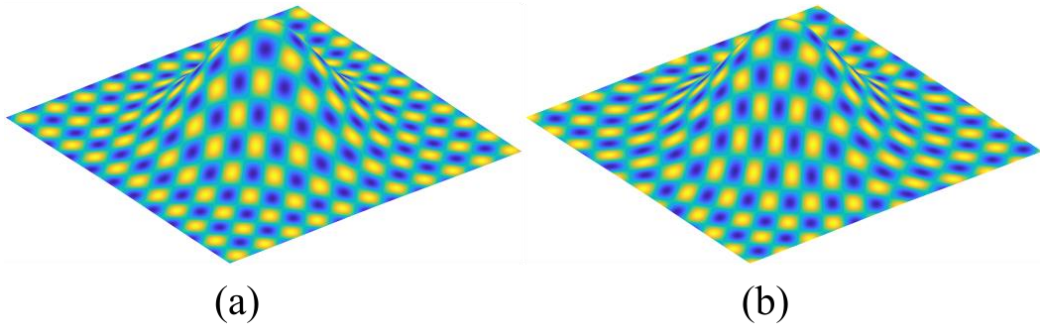

Figure 2.3 (a) SVL on a Gaussian surface with no deformation control. (b) Same surface after performing deformation control.

2.4 Object Placement, File Export, and Array Generation

To build a FSS array, the intersection of the two planar gratings is scanned for maxima. The locations of these maxima are stored in a separate array. The FSS element was modeled in CAD and exported as a standard tessellation language (STL) file format. The element STL was imported into MATLAB and placed at each of the maxima identified previously. For the FSS array to be built properly, elements could not be placed flat at the location of the maxima. In addition, it was found necessary for the elements to be oriented at an angle tangential to the surface. This was accomplished by calculating the vector normal to the surface at the location of the maxima and rotating the element to match the direction of the normal vector. All of the elements are combined and exported as a single STL file. This entire process is outlined in Figure 2.4 with a randomly generated surface used as an example.

The oriented elements shown in (c) still show some of the elements intersecting with the surface where the surface curvature is more severe. To fix this, the surface and the array of elements were imported into the open source modeling software Blender. The array of elements was conformed perfectly to the surface using Blender's shrink-wrap modifier. The final array and surface are exported as separate STLs from Blender. The final result is shown in (d) with the elements flushed to the surface.

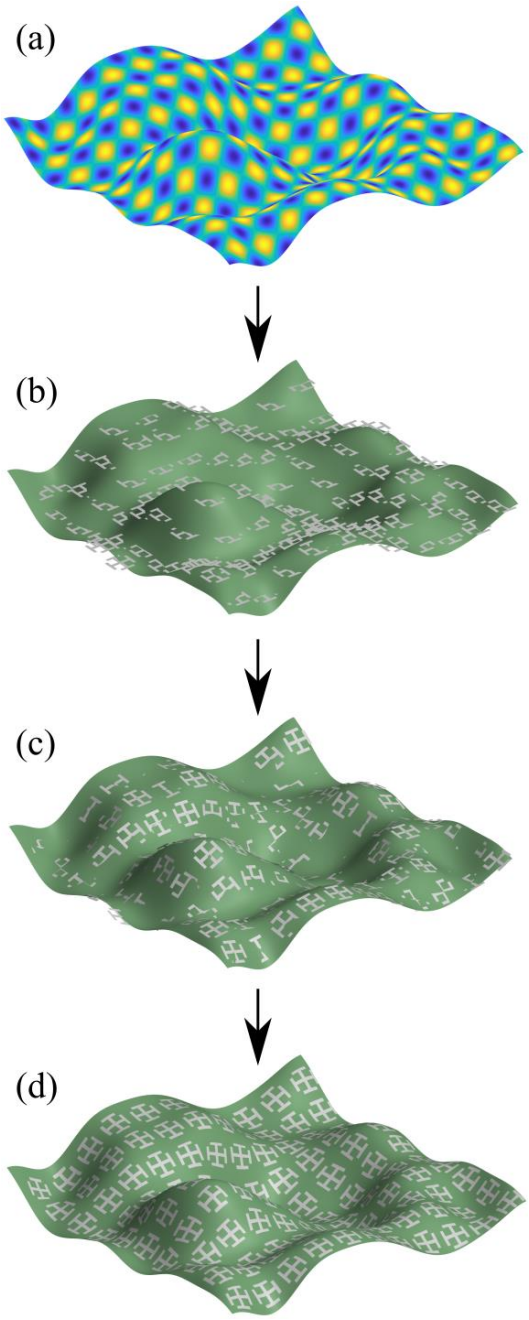

Figure 2.4 (a) SVL generated across random curvature resulting from the sum of two planar gratings. (b) FSS elements placed flat on the location of the maxima. (c) Elements oriented tangential to the surface still showing some intersections with the surface itself. (d) Elements shrink-wrapped to the surface using Blender.

Chapter 3: Hybrid 3D Printing and Preliminary Devices

3.1 Hybrid Printing Systems

All of the hybrid 3D printing processes presented were primarily applied using two printing systems. Two nScrypt 3Dn-Tabletop printers are shown in Figure 3.1. Both printers share identical chassis and basic tools. They are both outfitted with a thermoplastic extruder (nFD™) and a micro-dispensing head (Smartpump™). Both the nFD™ and Smartpump™ use ceramic pentips of varying sizes. Table 3-1 summarizes common sized pentips. In total Tabletop #1 includes a broad set of tools such as a 200W laser, a 40 W laser, a fiducial camera, a surface Z-scanner, an nFD™, and a Smartpump™. Tabletop #2 includes a more modest number of tools outfitted with only an nFD™, Smartpump™, and basic camera. In contrast to Tabletop #1, Tabletop #2 has a larger docking bay capable of fitting up to 4 toolheads. Any combination of nFD™ and Smartpump™ toolheads can be used. This work, however, was limited to the use of only a single nFD™ and a single Smartpump™.

Table 3-1 List of standard pentip sizes for nScrypt tabletop systems.

Pentip Sizes (Inner Diameter - ID)
10µm, 15 µm, 25 µm, 50 µm, 75 µm, 100 µm, 125 µm, 200 µm, 300 µm, Custom*

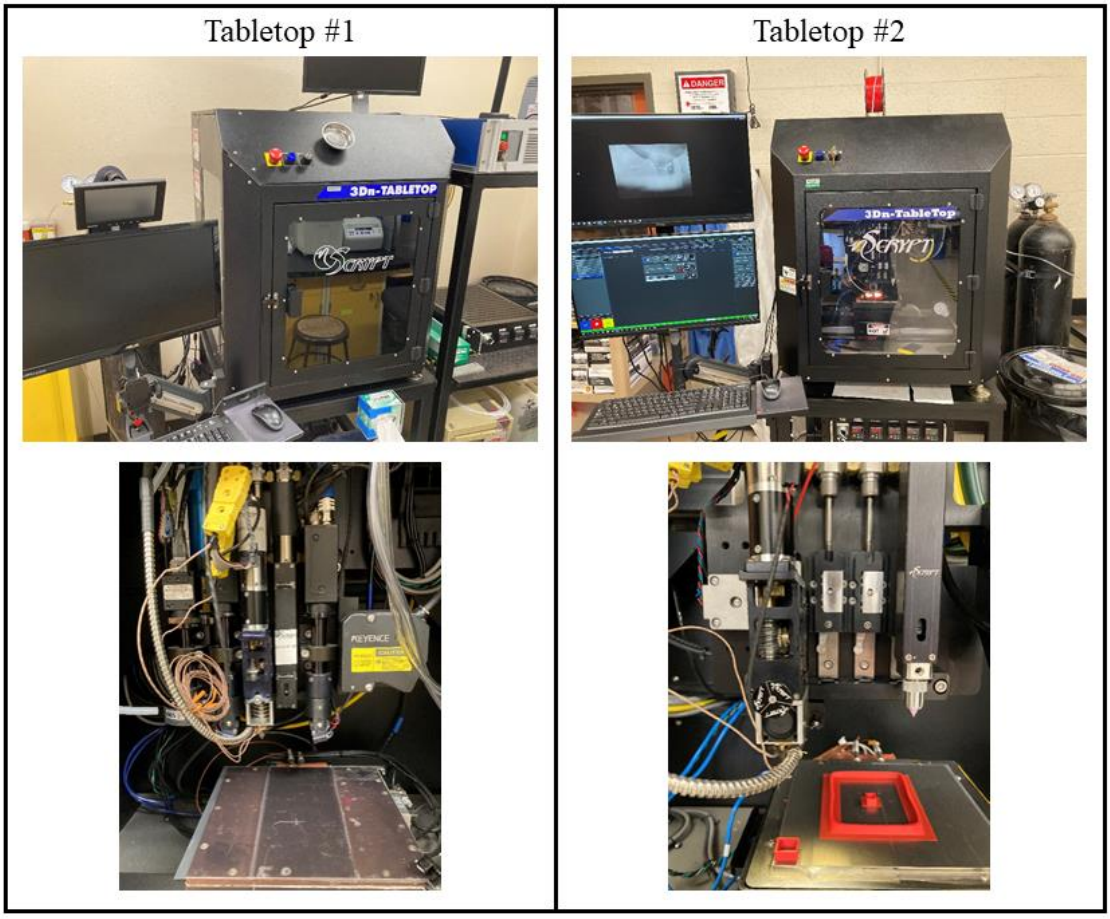

Figure 3.1 (Left) nScrypt tabletop system #1. (Right) nScrypt tabletop system #2.

Before printing can begin, several best practices related to system preparations are made. There is a fair amount of literature available regarding these steps [77, 78]. As a result, some of these steps will only be listed here. In general, it is good practice to:

- Select appropriately sized pentips depending on the scale of the print job
- Maintain a clean printing environment
- Minimize moisture content in the filament used by baking the filament
- Properly load CB028 (or other conductive pastes) in syringes minimizing air bubbles and ensuring homogeneity

- Calibrate the system each time a new toolhead is added and/or each time a pentip is changed
- Find Smartpump™ valve open and close position

The most crucial step in hybrid 3D printing is system calibration. During system calibration a world floor value is found. This value is the absolute lowest point each individual toolhead can travel in the negative z-direction before crashing onto the printing surface. This value will vary between printing systems and will even vary slightly between toolheads inside the same printing system. The world floor value is also dependent on the pentip used. In general for an nScrypt system, pentips with a larger diameter will sit higher than a pentip with a smaller diameter. Calibration entails not only finding the differences in the tool's height along the z direction, but also finding each tool's position in the x and y directions relative to each other. Accurately finding these positions will allow the user to correctly align the paths when printing in a volumetric hybrid process. For this work only two printing heads are used. The differences in position are calibrated and wrote down manually. These values are then used as an input for the slicer that will generate the machine code necessary to run the hybrid printer. For the rest of this work, calibration was done multiple times to ensure as accurate a print job as possible.

3.2 Printing Parameters and OmniSlice™

All of the world's printing procedures, best practices, and various hybrid printing systems would be of no use without a modern slicer. The slicer used in this work, called OmniSlice™, is a revolutionary slicer that is commercially available [79]. In original works, the slicer shown in [29] was a simple 1-to-1 translation of a dual filament print job with the g-code being completely generated by open source software Slic3r. The printing paths corresponding to the second material were then modified to account for the change in physics involved in the dispensing of

conductive pastes when using the Smartpump™. This work proved a lot of concepts and generated the world's first volumetric circuits and meandering radio frequency (RF) interconnects. However, this work had several limitations. It was limited to only work on nScrypt tabletop models and its g-code generation was controlled solely within open source software Slic3r. It could also only generate dual material print jobs (1 nFD™ and 1 Smartpump™). In contrast, OmniSlice™ is a standalone tool. It is system agnostic and can generate printing paths for an unlimited number of toolheads and toolhead combinations. It is also fully customizable capable of being modified to generate toolpaths for any custom dispensing apparatus. Toolpaths are uniquely tailored to their corresponding printing apparatus.

Table 3-2 shows a summary of example printing parameters used within a hybrid print job generated using OmniSlice™ for an nScrypt 3Dn-Tabletop using a single nFD™ in combination with a single Smartpump™. While not limited to these parameters, these parameters were chosen as the most critical for generating a successful print job using OmniSlice™. "Pentip diameter" is a parameter shared between the nFD™ and Smartpump™ and refers to the inner diameter of the selected pentip for each toolhead. Layer height is another common parameter and refers to the height of each layer along the z direction. This is the only parameter that must be the equal for all tools within the same print job. Linewidth refers to the width of each path on the x-y plane. In general, layer height and linewidth are inversely proportional to each other. The smaller the layer height, the closer the print head is to the bed plate (or the previously printed layer). This causes the printed line to be "ironed" or flattened against the printing surface in turn leading to larger linewidths. The maximum layer height is limited by the pentip diameter. The smallest linewidth capable of being dispensed is roughly equivalent to the pentip diameter. Perimeters (often referred to as shells) refer to the total number of outlines generated for a given feature.

This is a standard feature of all slicers where an outline is first generated for an object and is then "filled" in. Infill is then the value (percentage) that is filled within a given number of shells. 100% is then completely filled and in the opposite spectrum 0% generates only perimeters. Speed refers to the movement speed for each individual toolhead. Top and bottom layer count refers the total number of solid layers to be used for the top and bottom of the model respectively. These layers will be forced to be 100% infill. The extrusion factor is a parameter solely for the nFD™ or thermoplastic toolheads. It slightly adjusts the quantity of material being extruded to account for any over or under-extrusion. This value is generally kept within 0.9 and 1.1. If a plastic process needs further adjustment than those values then it is a good sign that the linewidth must be adjusted instead. Retraction distance and speed is another parameter only relevant to the nFD™. At the end of each toolpath the filament is retracted a certain distance and at a certain speed. This helps minimize any oozing that occurs in the nFD™. The last few parameters are only relevant to the Smartpump™. At the calibration stage before a hybrid printing process can begin, an open and close value is found for the Smartpump™. At the closed position value there is no flow of conductive paste and conversely at the opened value conductive paste flows at a desired rate. The "valve delta" is then the difference between the open and closed positions and tells you the total distance the valve must travel before it is considered "open." The "valve open/closed" speed is then how fast the Smartpump™ valve moves when opening and closing. Pressure is applied to a syringe containing a conductive paste. For the majority of hybrid prints in this work it can be assumed that Dupont CB028 is used. Many different forms of conductive pastes are available commercially. Lastly, perhaps the most critical parameter left for the Smartpump™ is the dispense gap. This value offsets the Smartpump™ paths along the z-direction with respect to the nFD™ toolpaths. This ensures that

conductive paste is always dispensed a certain distance above the plastic layers. It is noted here that this value is an overall z-offset. It accounts for both the layer height and a true dispense gap. In a typical flat 2D print job the dispense gap refers to the height above a substrate at which the conductive paste is dispensed. The term dispense gap is simply borrowed here.

Table 3-2 Hybrid printing parameters used for initial prints.

Parameter	nFD™	Smartpump™
Pentip diameter	125 µm	125 µm
Layer height	0.050 mm	0.050 mm
Linewidth	0.175 mm	0.175 mm
Perimeters	1	1
Infill	100%	100%
Speed	30 mm/s	15 mm/s
Top layer count	0	0
Bottom layer count	0	0
Extrusion factor	1	N/A
Retraction distance	3	N/A
Retraction speed	15	N/A
Valve open/close Speed	N/A	0.6 mm/s
Valve delta	N/A	0.042 mm
Pressure	N/A	10 PSI
Dispense gap	N/A	0.185 mm*

3.3 3D Printed Eyeglasses with Antenna

This project was taken in collaboration with Ball Aerospace and the Colorado School of Mines that focused on 3D printing a functioning RF device capable of operating at Wi-Fi/Bluetooth frequencies. The Colorado School of Mines was responsible for designing a pair of eyeglasses that contained a dipole antenna within one of the arms of the eyeglasses' frame. The School of Mines did all physical and electrical modeling. Printed iterations of the final design are shown in Figure 3.2. The design itself is a half-wave dipole printed on the yellow arm of a pair of eyeglasses. Although not a true 3D/volumetric design it is a good example of a functional wearable electronic device made solely through 3D printing. Manufacturing was all done using an nScrypt 3Dn-Tabletop printer with ABS as a dielectric and Dupont CB028 silver ink as a conductor. The

conductive paste was dispensed using a manual print job with a 100µm dispense height with respect to the printing surface. The School of Mines tested the device using facilities at Ball Aerospace in Boulder, Colorado. The assembled eyeglasses along with measured results are shown in Figure 3.3. This figure shows the reflection coefficient (or S11) using two separate feeding techniques. The device shows a resonant frequency at 1.8 GHz. Further tuning of this frequency can be done by trimming the length of the conductive paths. On the right is one the final assembled devices. The functioning arm was printed in yellow and conductive paths can be seen in silver.

Figure 3.2 Print iterations of dipole antenna on an arm for a pair of glasses.

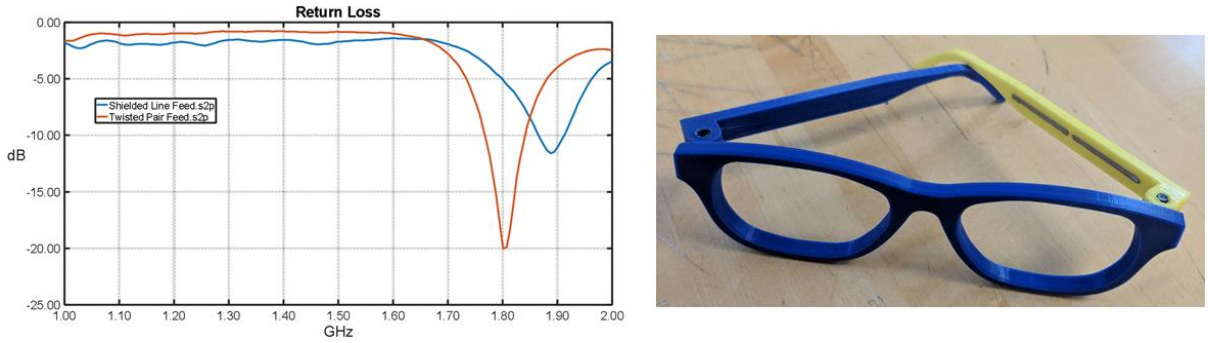

Figure 3.3 (Left) Return loss (S11) for two different feeding mechanisms. (Right) Complete set of eyeglasses, antenna arm shown in yellow.

3.4 U-Slot Patch Antenna on High-k Substrate

This was a follow on project on wearable electronics done again in collaboration with Ball Aerospace and the Colorado School of Mines. The goal of this project was to design and manufacture a wearable GPS antenna capable of tracking the user. The Colorado School of Mines was responsible for all the design aspects of the antenna and its housing. UTEP's EM Lab was responsible for all manufacturing. A novel aspect of this antenna design was the use of a substrate with a high dielectric constant. Premix Preperm ABS1000 with a dielectric constant of 10 was the commercially available solution used. The higher dielectric constant compared to regular ABS plastic allowed the antenna dimensions to be scaled down to a reasonable size.

First, the dielectric constant was measured using a Damaskos Model 125HC thin sheet dielectric tester. Three thin sheet samples with a thickness of 0.6mm were printed using a Makerbot Replicator 2X. The samples were printed using 100% infill to ensure the highest possible loading. The samples along with the measured relative permittivity and loss tangent are shown in Figure 3.4. Although the loss tangent was close to specifications, the highest dielectric constant measured had a value of 7.6. An average of the three measured values was used for the final antenna design.

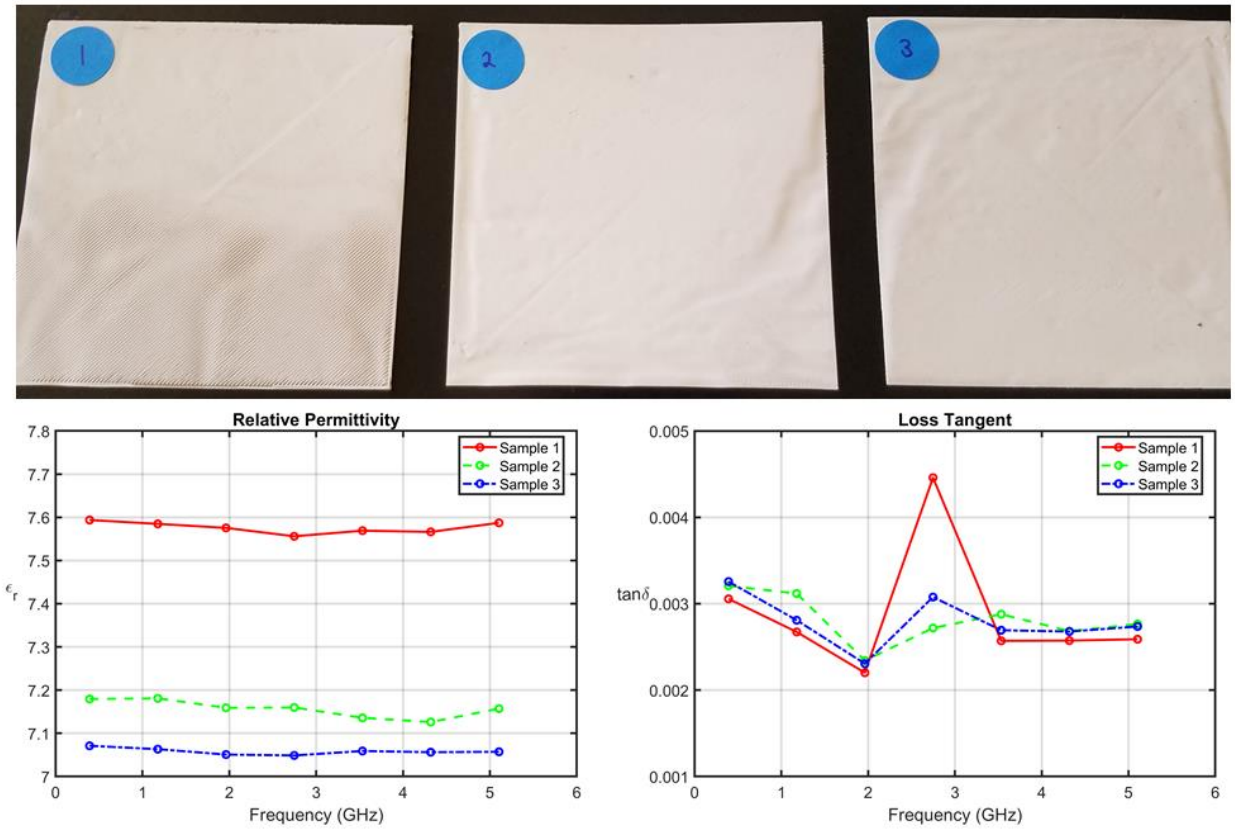

Figure 3.4 (Top) Three thin dielectric sheets tested for relative permittivity and loss tangent. (Bottom) Measured relative permittivity and loss tangent.

The final antenna design featured a u-slot patch antenna manufactured using an nScrypt 3Dn-Tabletop printer with Preperm ABS1000 used as the substrate and Dupont CB028 used for the conductors. Preperm ABS1000 was printed with a 0.4 mm pentip at a temperature of 250°C. A 100µm dispense gap was used to print the conductors. A large dispense gap was used to keep the Smartpump™'s pentip from dragging along the substrate's uneven surface. The final design and its measured results are shown in Figure 3.5. Not pictured are an SD card reader, an ATmega328, GPS receiver, and battery pack inside the red PLA housing. The PLA housing itself was printed separately using an Ultimaker3.

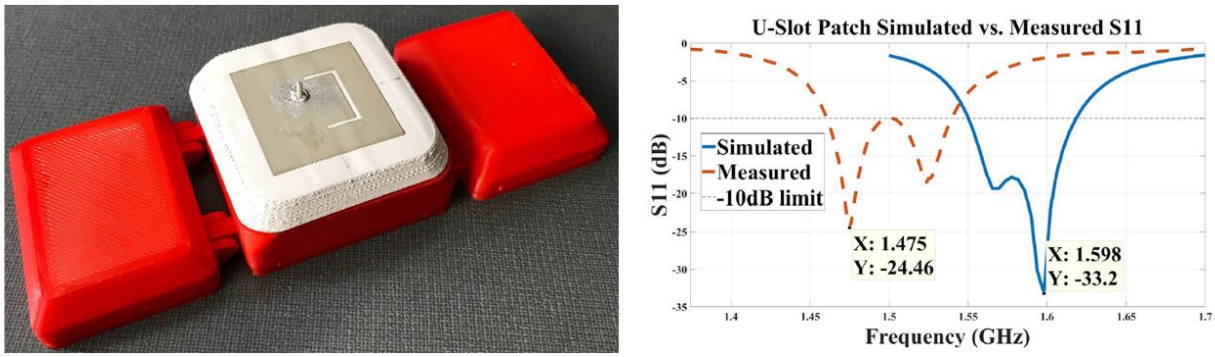

Figure 3.5 (Left) Final tested device featuring u-slot antenna on hi-k substrate atop of red PLA housing. (Right) Simulated and measured return loss.

The measured reflection coefficient showed a frequency shift of approximately 100MHz. This shift can be explained by the substrate having a slightly higher dielectric constant than what was expected from measurements. While measured results did not reach the specified dielectric constant of 10, Preperm ABS1000 was found to be a suitable commercially available solution for a high dielectric constant thermoplastic that can be printed relatively without issues. Its applications in 3D printing or antenna engineering vary. In this work, a higher dielectric loading on the antenna's substrate was used to miniaturize the antenna's physical dimensions. Other applications, such as metamaterials, that combine the use of both ABS plastic and Preperm ABS1000 in a dual filament print job can also be explored.

3.5 World's First 3D Volumetric Circuit via Automated Manufacturing – Holey Frijole

The two previous devices were good examples of standard hybrid printing processes. Recently, the world's first 3D/volumetric circuit was printed using a true hybrid 3D printing process [28]. In a true 3D/volumetric circuit components can be placed in any position throughout all three dimensions as well as in any orientation. Interconnects can meander smoothly throughout the circuit following spline-like paths. This design was then modified to a more arbitrary shape affectionately called the "holey frijole" shown in Figure 3.6. The circuit

itself is a simple model that implements the use of a 555 timer to flash an LED light. This success was made capable by 3D printing software developments. First a design must be created in a 3D environment via the use of a 3D layout tool. Within this tool circuit components are placed in any desired position and orientation. This tool also exports the necessary standard tessellation language (STL) files for 3D printing. These files are then sliced using a hybrid slicer that translates these files into the code necessary to drive the 3D printer [29].

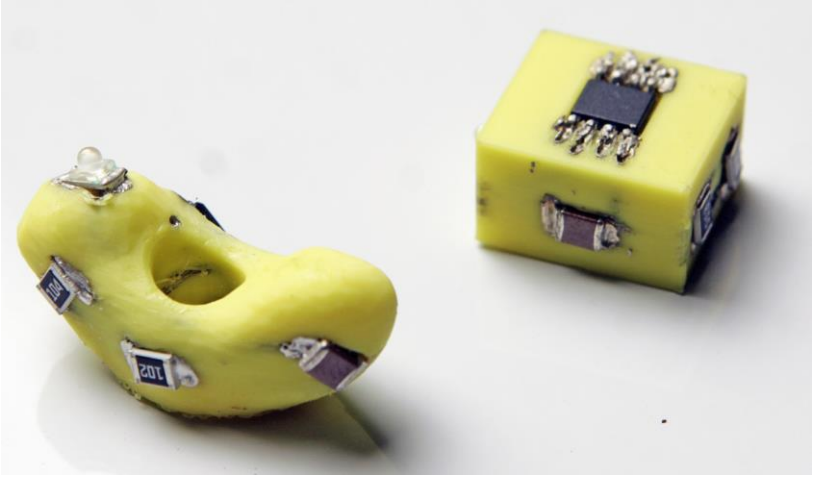

Figure 3.6 Holey frijole and original cubic 555 timer 3D circuit.

The slicing parameters shown in Table 3-2 were used for both original 3D/volumetric circuit and the holey frijole. The combination of the hybrid slicer and 3D circuit layout tool was the first time demonstrating a true hybrid 3D printing process capable of manufacturing any arbitrary arrangement of metals and dielectrics. It was at this early stage the some of the first best practices and design rules for hybrid printing were developed. Of note, are the differences in print speeds for each toolhead. Initially it was expect that the Smartpump™ should move at a speed equal to or faster than the nFD™. In a traditional 2D print, planar structures are typically printed at a faster rate in order to have as thin as layer of conductive paste as possible. In a hybrid printing process, the opposite was found. Since the spline paths connecting each component are cylindrical in nature and therefore volumetric a lower speed was needed to ensure

a sufficient amount of conductive paste was dispensed in each cavity. To maintain a high conductivity, it is then critical to ensure the diameter of these cavities is as low as possible. Further design rules and best practices will be developed throughout this work.

3.6 World's First 3D Volumetric Transmission Lines – Parallel Plate Transmission Lines

The holey frijole was designed to only function using direct current (DC). A logical next step was then to design interconnects capable of working at higher radio frequencies (RF). The majority of this work was disclosed in [77]. Therefore, only direct contributions will be summarized here. The ideal transmission line is composed of at least two conductors and transmits 100% of input power for all frequencies (assuming no material losses). In a traditional RF circuit, the most commonly used transmission line is the microstrip transmission line (MTL). The design of a MTL includes a large ground plane which is incompatible with 3D/volumetric design as a plane is an inherently 2D concept. Instead, the parallel plate transmission line (PPTL) was proposed as a candidate for 3D RF interconnects. This design consisted of two finite sized plates separated by a small distance and was capable of being twisted and routed arbitrarily throughout a volumetric circuit.

In order to classify the PPTL as a 3D transmission line, several fundamental bend types were identified: (1) straight PPTL (2) in-plane bend (3) out-of-plane bend and (4) barrel roll. An actual 3D/volumetric PPTL in a circuit may be composed of a combination of all these fundamental bend types. These models are shown in Figure 3.7 along with their respective simulated results. All models were simulated in Ansys HFSS with a rectangular waveport used as the source of excitation. Lossless materials (perfect electric conductors) were used. It was

observed that for minimal bend radius, all fundamental bent types were capable of transmitting close to 100% of input power.

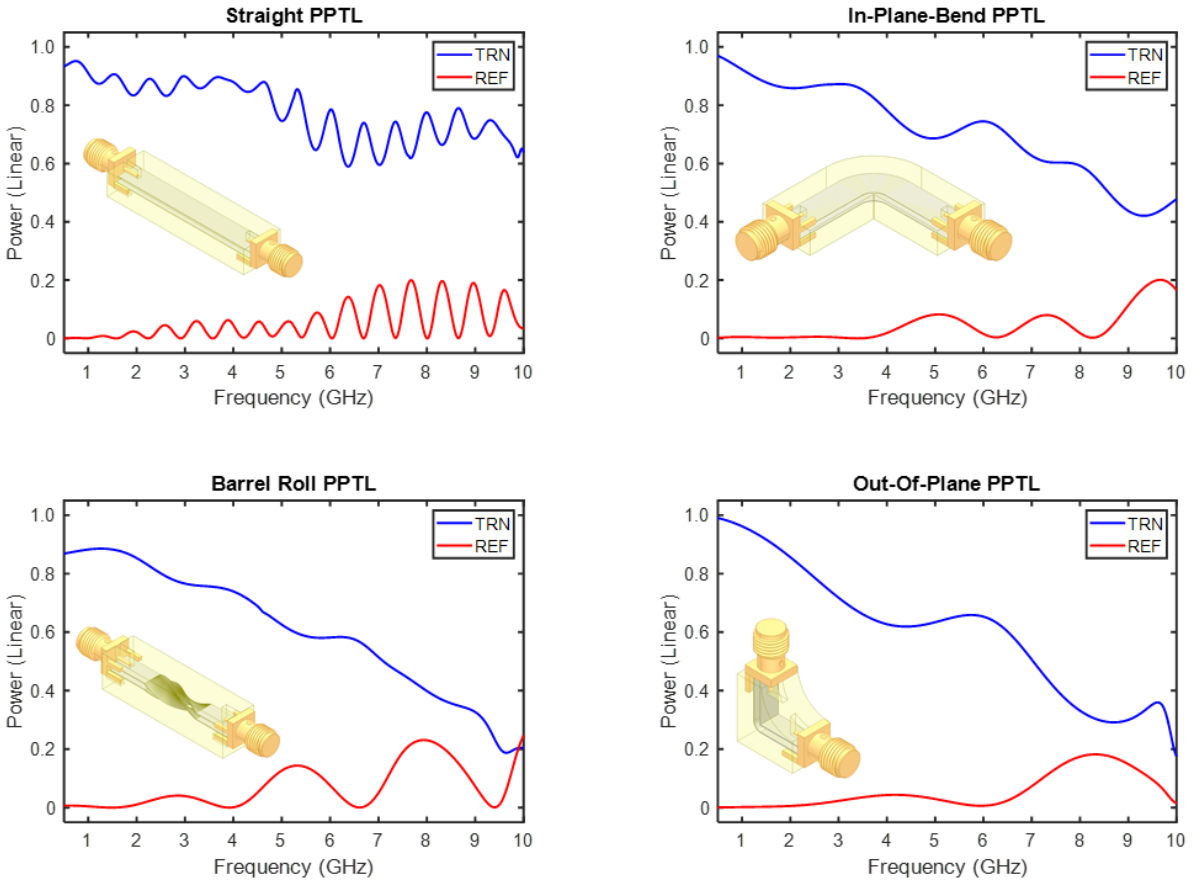

Figure 3.7 (Top left) Straight PPTL embedded in ABS. (Top right) In-plane-bend PPTL embedded in ABS. (Bottom left) Barrel roll PPTL embedded in ABS. (Bottom right) Out-of-plane PPTL bend embedded in ABS.

These four bend types were hybrid printed using Tabletop #1 with the same parameters shown in Table 3-2. An Amphenol RF 132322 connector with a 50 Ω impedance is attached at each end of all PPTLs in order to measure both transmission and reflection. The hybrid printed PPTLs are shown in Figure 3.8. The PPTLs were measured at the EM Lab using an Agilent N5245A PNA-X Vector Network Analyzer. The measured results are shown in Figure 3.9. It was noticed here that all PPTLs greatly deviate from an ideal transmission line behavior. Simulations were updated to include the effect of the SMA connectors and a majority of the

losses were explained through the modal mismatch between the coaxial mode of the SMA connector and the mode within the PPTLs input/output faces. It was concluded that a new connector, compact balun design, or perhaps an entire new transmission line design will be necessary for 3D/volumetric circuits.

Figure 3.8 Starting from the left, fabricated straight PPTL, in-plane-bend, barrel roll, and out-of-plane bend.

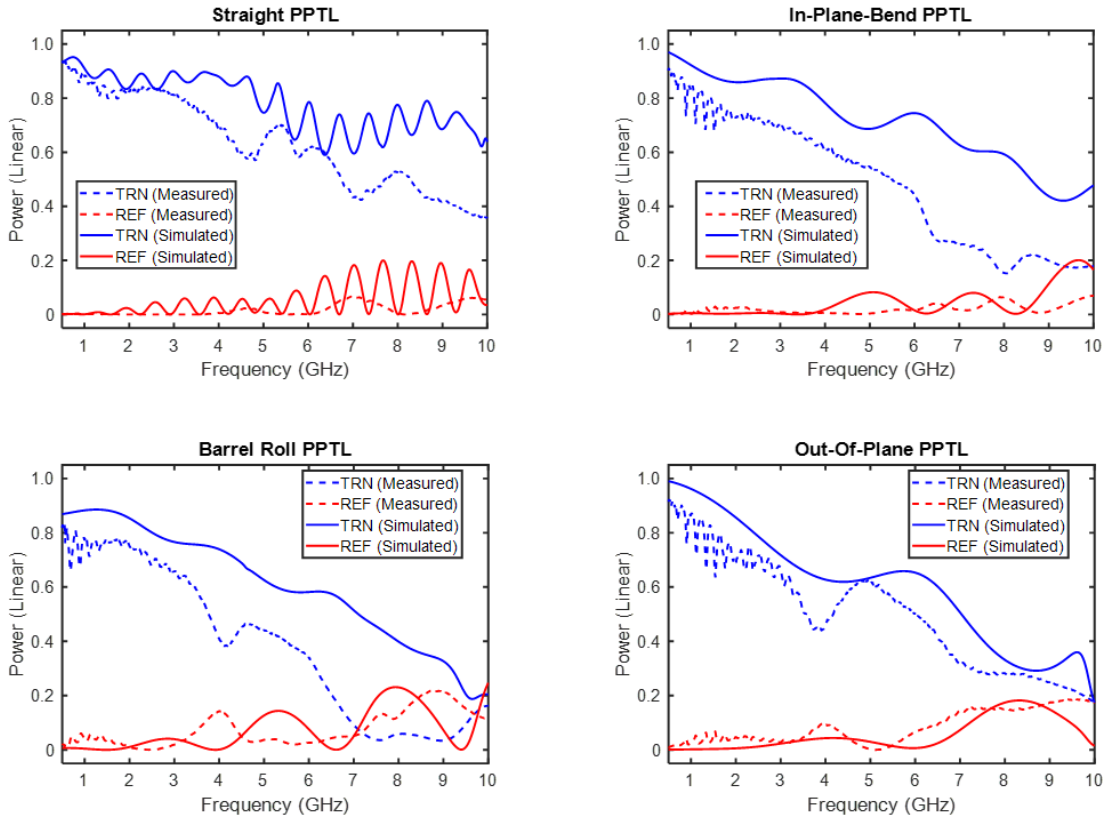

Figure 3.9 Measured results for all PPTLs.

Chapter 4: Conformal Frequency Selective Surface on Doubly Curved Surface

In this chapter, the conformal SVL algorithm for conformal FSSs on arbitrary curvature described in Chapter 2 is implemented and verified. To demonstrate the algorithm's capability of conforming FSSs to curves and preserving their electromagnetic performance, an array composed of Jerusalem cross (JC) elements was generated. This element was chosen for several reasons: its popularity and extensive use in literature [80]-[82], less sensitivity to polarization and angle of incidence, relatively complicated geometry to exercise the algorithm, and its sensitivity to size and shape make it suitable for demonstrating the conformal SVL algorithm. The curve the array was conformed to follow a tall parabolic dome of non-equal *x* and *y* axes. This doubly curved surface was chosen as an extreme case capable of demonstrating the robustness of the SVL algorithm. This chapter will thoroughly describe the process of generating a FSS conformed to a curved surface beginning with simulations at the infinite array level followed by finite array simulations. All electromagnetic simulations in this chapter were carried out using commercial software Ansys HFSS. Lastly, three arrays were manufactured and measured. A standard flat array, a projected curved array, and an array conformed using the conformal SVL algorithm.

4.1 Infinite Array Simulations

A model of the JC unit cell that will be used is shown in Figure 4.1. For simulation, primary/secondary boundaries were used to effectively model an infinite array. A Floquet port was used as the source of excitation to launch a linearly polarized mode traveling in the negative *z*-direction. Perfect electric conductors along with a dielectric constant of $\varepsilon_r = 2.5$ for the substrate were used. The design approach for this unit cell focused on two things:

- Frequency of operation in the X-band (8.2GHz – 12.4GHz)
- Feature sizes that could be easily manufactured (~1mm minimum in width)

The period chosen was 9.95 mm in both directions (square symmetry). This period was found to have single order mode operation in the given frequency range. Once the period was selected, all the dimensions were scaled until the first resonance was located at approximately 10 GHz. After scaling, the smallest dimension found had a value of 0.9 mm and still within a reasonable manufacturing size.

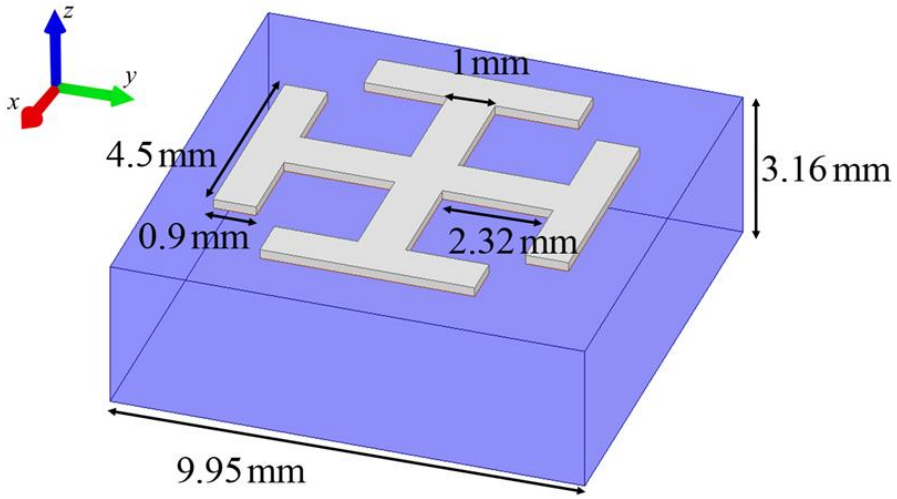

Figure 4.1 JC element model

Simulated results are shown in Figure 4.2. Due to symmetry, both linear polarizations (+*x* and +*y* directions) exhibit the same response, therefore only one is shown. As expected, this particular element shows a strong reflection at approximately 10 GHz and operation in the X-band frequency range. This JC model was exported from Ansys HFSS using the initial graphics exchange specification (IGES/IGS) file type. The IGS file was then converted to a faceted model, cleaned, and remeshed in Ansys Spaceclaim. The final model was exported as an STL file from Spaceclaim and used for generating the final conformal model using the process outlined in Chapter 2.

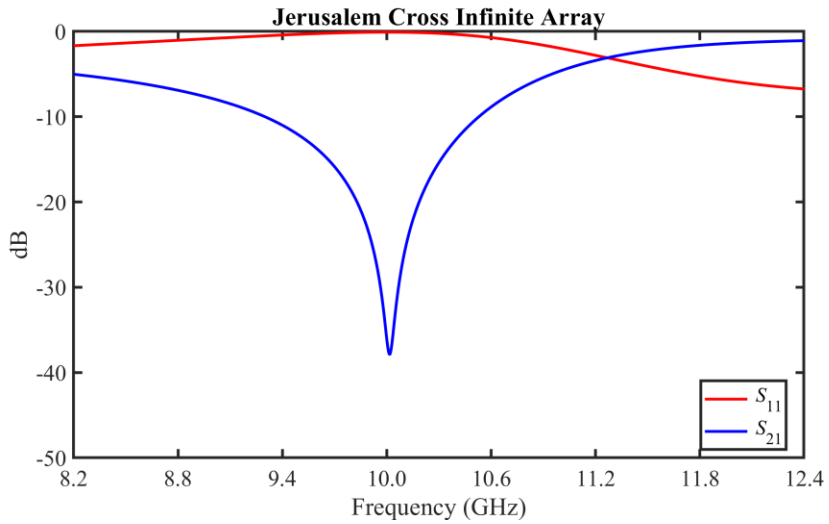

Figure 4.2 Simulation of infinite array of JC. A reflection band was observed at 10 GHz.

4.2 Finite Array Simulations

Following the simulation of an infinite array, simulations for more realistic finite arrays were carried out. These simulations were also done in Ansys HFSS with the set-up for all three shown in Figure 4.3. A flat 10×10 array of JC elements is shown on a 99.5 mm × 99.5 mm surface, the same array projected onto a parabolic dome, and lastly the same array as generated by the conformal SVL algorithm. As previously mentioned, operation in the X-band was desired. The simulation space created was made to emulate a measurement set-up. Horn antennas modeled after Arra Inc WR90 were included. A 60 mm gap between both horn antennas was kept for all simulated models. Waveports were used as the form of excitation designating one horn antenna as transmitting and another as receiving. The mode of excitation was linearly polarized along the $+x$ and $+y$ directions by alternating the orientation of both horns.

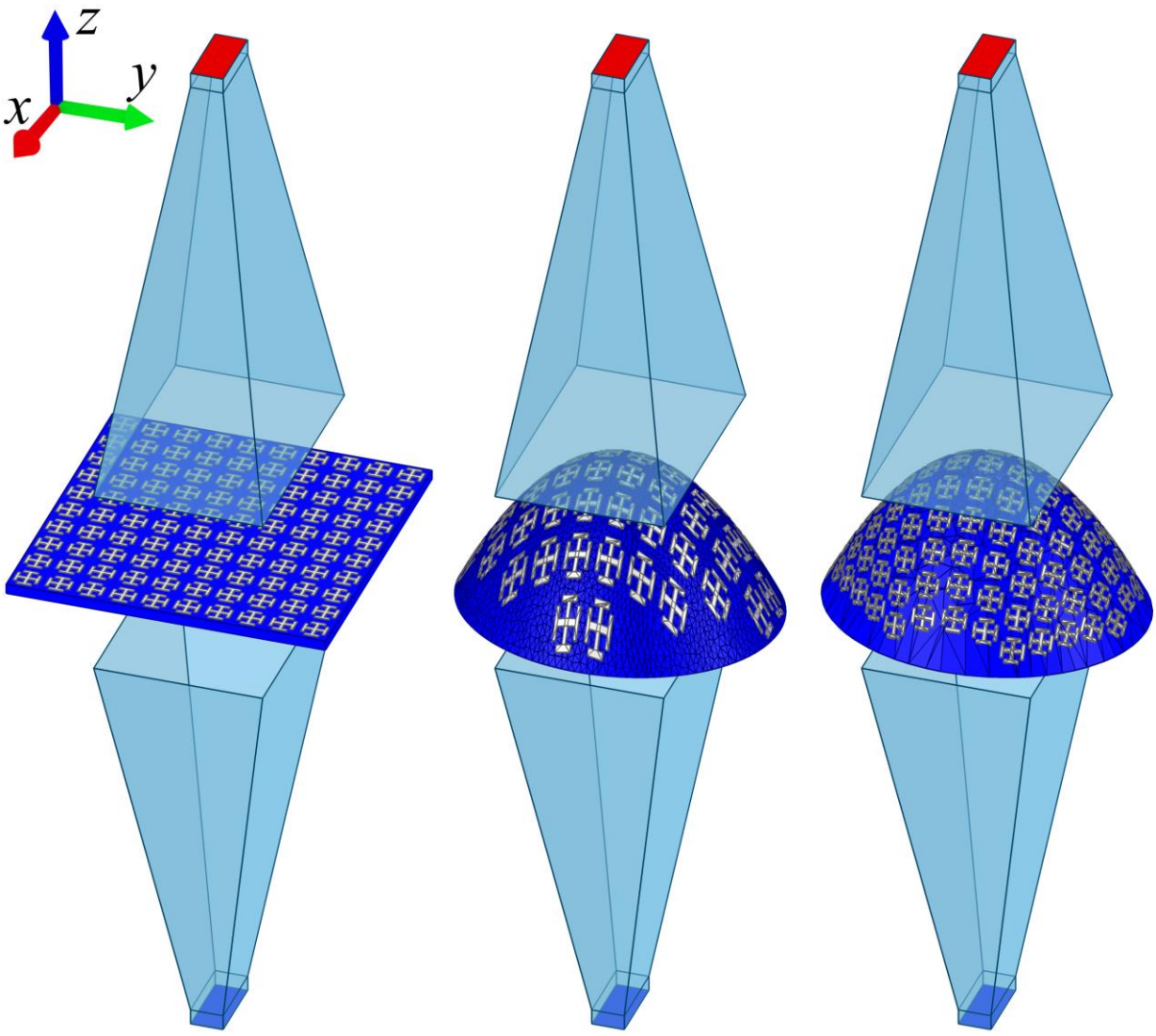

Figure 4.3 Simulation setup shown for all three FSSs. Not pictured are absorbing boundaries that enclose each of the three separate simulation spaces.

Careful consideration was taken to determine the total amount of JC elements and substrate size relative to the horn antenna's physical aperture needed to achieve a proper response from the device. Using the same simulation setup shown in Figure 4.3, finite array simulations were done for a flat substrate starting with a 2×2 (4 total elements) array of JC followed by 4×4 (16 total elements), 6×6 (36 total elements), 10×10 (100 total elements), and finally 14×14 (196 total elements). No resonant behavior was observed for both the 2×2 and 4×4 devices. A strong resonant response, however, was observed starting at 36 total elements with a substrate size of 59.7 mm ×

59.7 mm. This was compared to the horn antennas physical aperture which measured at 52.72 mm × 76.43 mm. The response remained unchanged up to 196 total elements. It is concluded that 36 elements at minimum and a substrate size of at least 59.7 mm × 59.7 mm will provide a resonant response for this particular element with the given dimensions. For the flat array, 10×10 total elements was chosen as more than sufficient.

A closer look at the arrays on a parabolic dome are shown in Figure 4.4. The overall area of the parabolic domes is the same for both at 81.24 mm × 100 mm. Their physical sizes are well above what is necessary for a proper response. For the first dome, a conventional approach was followed where a flat array was projected onto the dome. This was done by projecting the z values of the JC elements onto the surface itself and shrink-wrapping the projected JC elements onto the dome in Blender. The second array was generated using the conformal SVL algorithm described previously. The projected array contains 52 total elements compared to the SVL array that contains 109 total elements. This confirms the conformal SVL algorithm produces a much more efficient layout of elements. Both numbers are well above the minimum necessary for a strong frequency response. The discrepancy in total element count was found necessary so that the substrate for both arrays maintained the same physical dimensions.

The models were imported into Ansys HFSS as two STL files: one file for the dome itself and another for the array of JC elements. For the projected dome, noticeable deformation to the elements was observed despite having no visible deformation from the top view. The steeper the slope and more abrupt the curvature, the more deformed the FSS elements will be when projected. In comparison, the SVL FSS does not distort the elements while also maintaining the overall periodicity of the array. The simulated results for all three are provided in Figure 4.5.

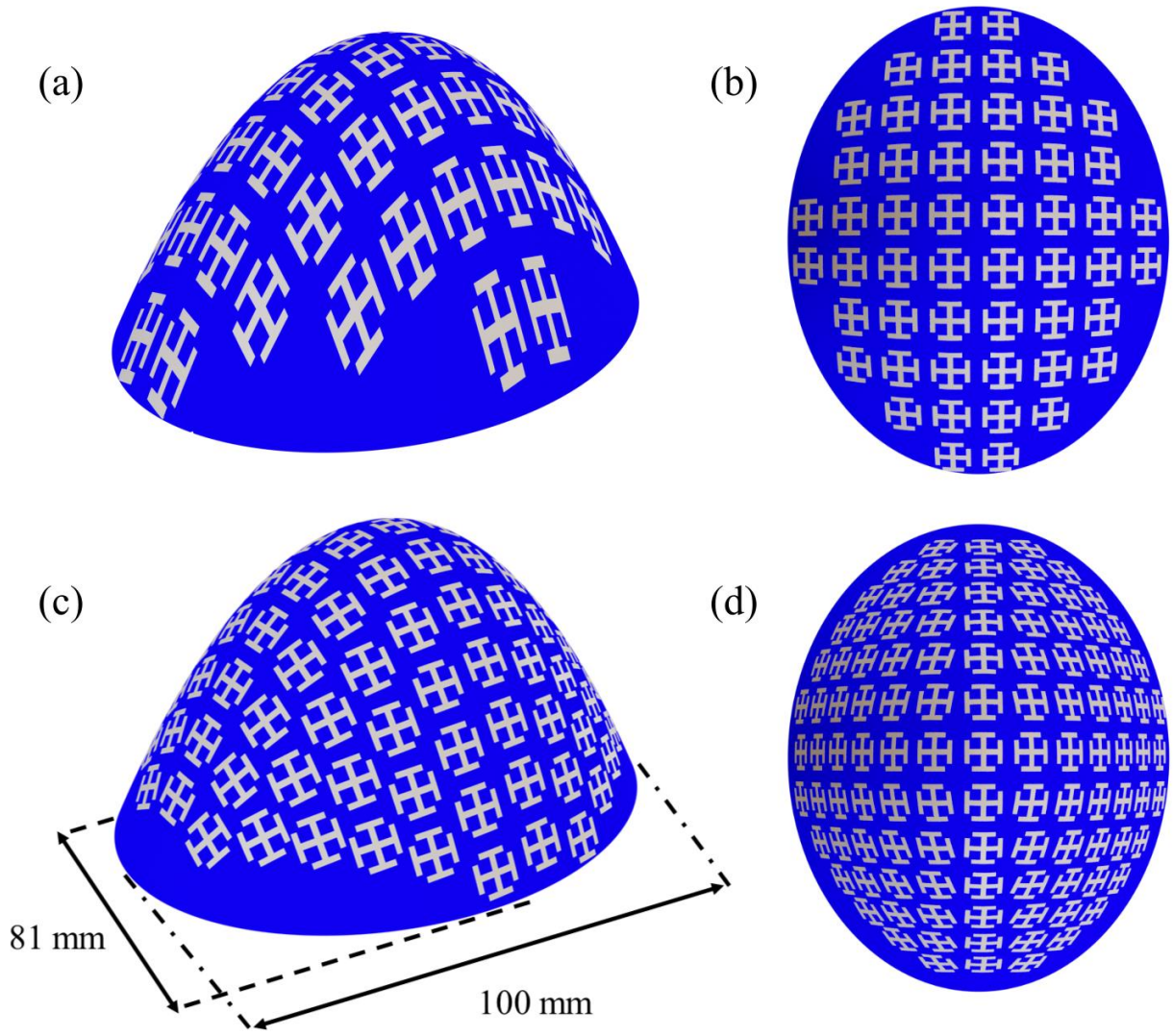

Figure 4.4 (a) Model for a JC FSS array projected onto a parabolic dome. (b) Top view of projected array. (c) Same array generated by conformal SVL algorithm. (d) Top view of array generated by conformal SVL algorithm. Both domes are 53 mm tall and of equal dimensions.

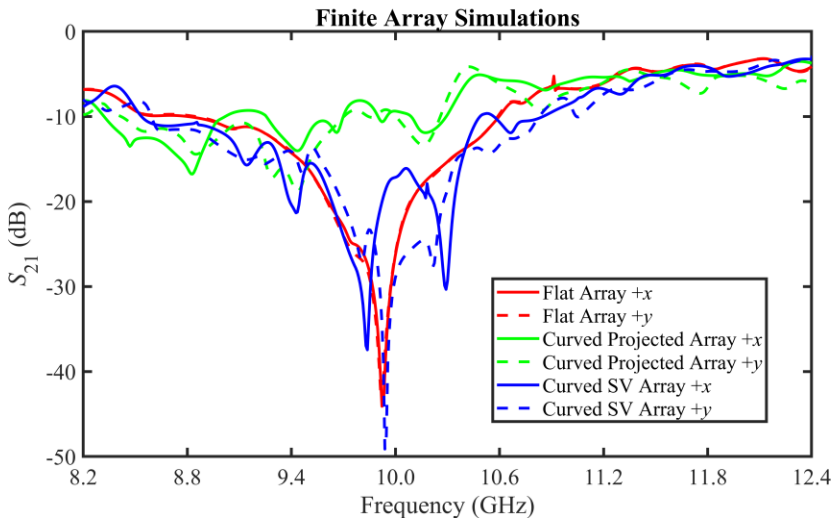

Figure 4.5 Finite array simulations of the three arrays. Flat 10×10 array results are shown in red lines. Results for the curved projected array are shown in a green lines. Lastly, results for the surface generated using the conformal SVL algorithm are shown in blue lines.

As seen in Figure 4.5 the finite flat 10×10 array exhibits a dip in transmission S_{21} at 9.92 GHz for a linearly polarized mode along both the +*x* and +*y* directions. The curved surface containing the projected array does not exhibit a response for any polarization due to deformations of the elements. In contrast, the curved SVL array exhibits a strong response at 9.84 GHz for a wave that is linearly polarized along the +*x* direction and at 9.94 GHz for a wave that is linearly polarized along the +*y* direction. Along with a 0.1 GHz shift, a secondary resonance was observed primarily for a mode polarized along the +*x* direction. These effects were caused by the incident wave exciting multiple polarizations on the curved SVL FSS. To explain this, a visual representation is shown in Figure 4.6. For both polarizations, the wave incident on the curved SVL FSS excites a combination of transverse electric (TE) and transverse magnetic (TM) polarizations over a continuum of angles of incidence. For a +*x* linearly polarized wave, the response is dominated by the TM polarization because it is TM along the broader side of the surface. For a +*y* linearly polarized wave, the response is dominated by the TE response

because it is TE along the broader side of the surface. Regardless of the polarization of the source wave, the resulting response is always a combination of TE and TM over a range of angles of incidence. To confirm this, infinite array simulations at varying angles of incidence were done. The angle of elevation θ was varied from 0° to 75° and the azimuthal angle ϕ was varied from 0° to 45°. These results are shown in Figure 4.7. While the Jerusalem cross element is known for having a robust response to angle of incidence, it was found that the resonance could shift up to 453.6 MHz for the TE polarization and up to 550.2 MHz for the TM polarization for larger angles of elevation for a flat infinite array. These same shifts were observed for the SVL array due to the curvature producing different angles of incidence across the surface. Thus, the response from the SVL FSS was consistent with simulations of the flat FSS, but averaged over a continuum of polarizations and angle of incidence. The SVL method is solely a geometry tool, capable of preserving the size, shape, and spacing of the elements to preserve the electromagnetic properties. Element designs that offer better robustness to angle of incidence would lead to conformal FSS arrays that offer the same improved performance.

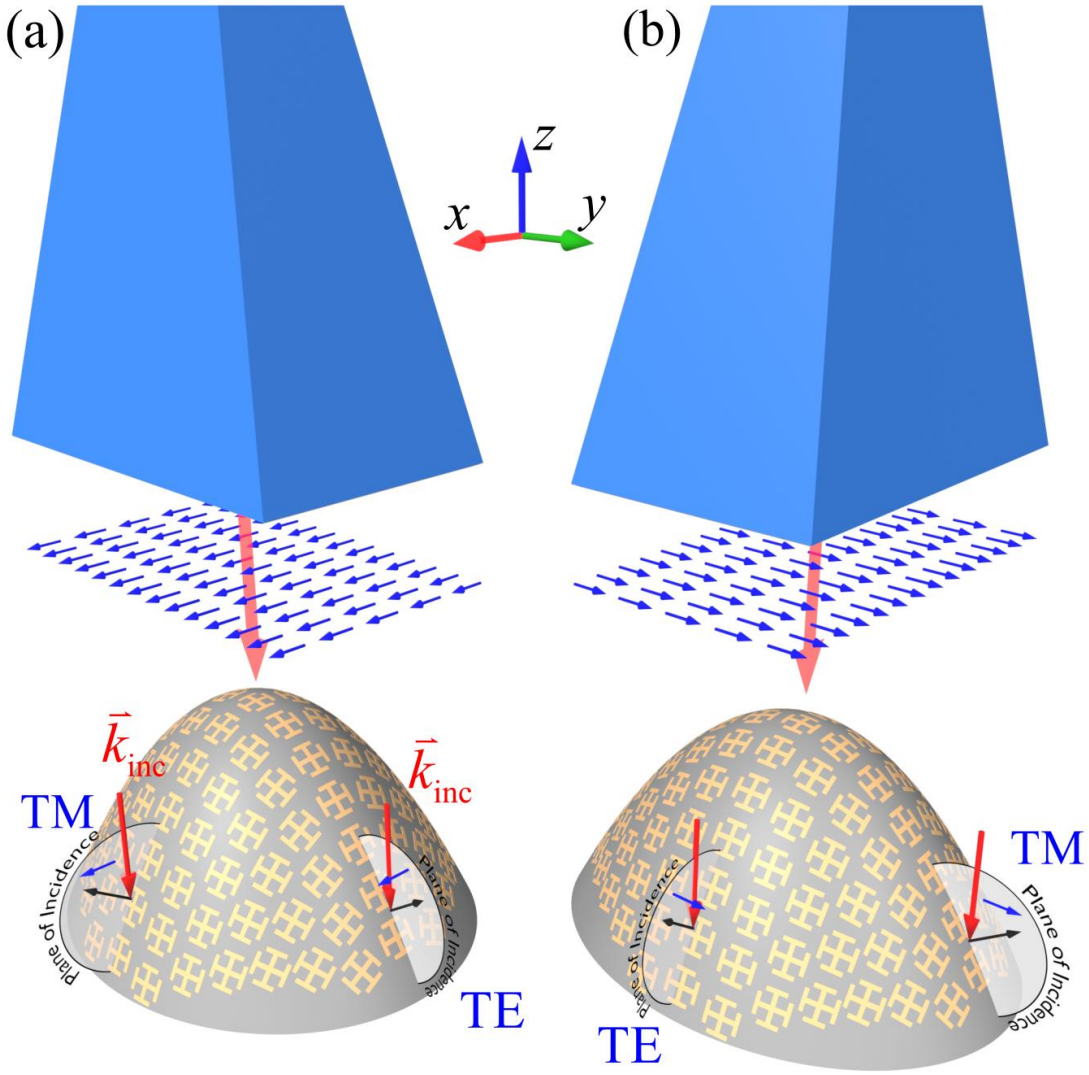

Figure 4.6 (a) Representation of a linearly polarized mode along the +*x* direction. (b) Representation of a linearly polarized mode along the +*y* direction.

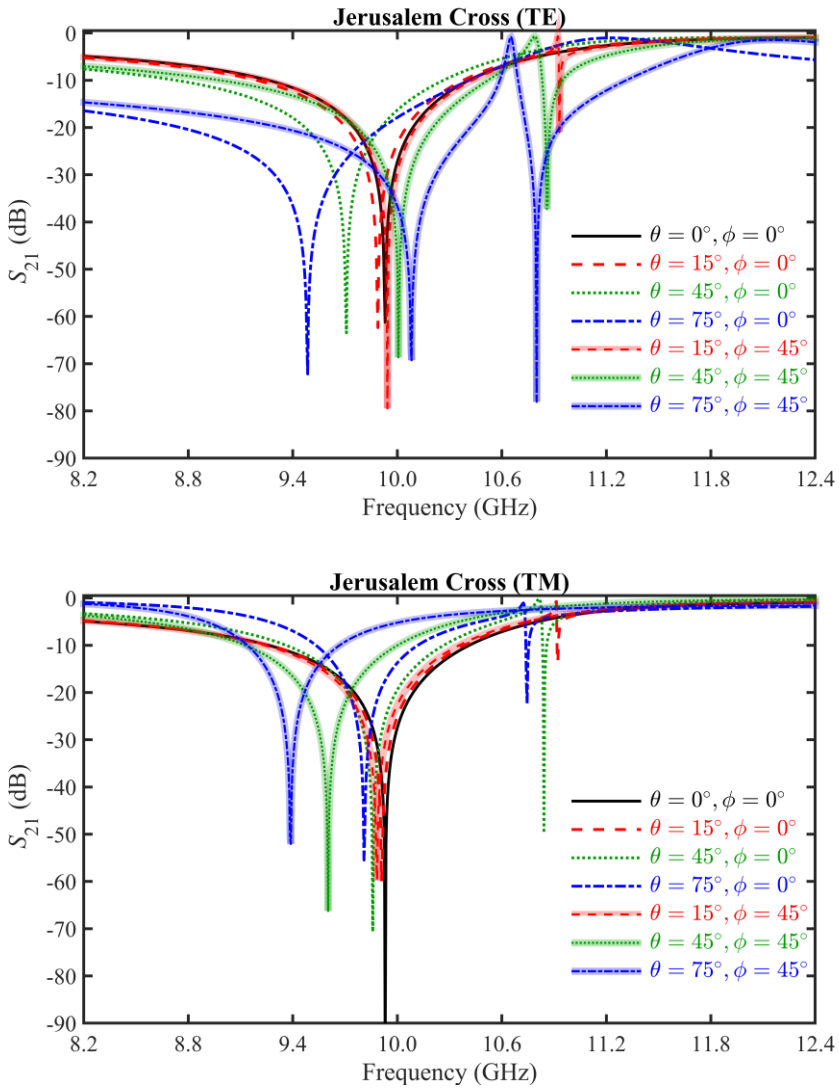

Figure 4.7 (Top) TE response for a JC infinite array. (Bottom) TM response for a JC infinite array. Response at normal incidence was independent of ϕ for both polarizations therefore it is not specified.

4.3 Corrected Element Design

Using STL files as the output of the algorithm makes them suitable for 3D printing. The file describing the curved surface was used to print the curved substrate while the second file containing the conformal array was used to print the conductive components. This is well suited for hybrid printing approaches or electroplating. At the time of this research, hybrid 3D printing of conformal structures was not available. As an alternative, it was simple enough to place copper

tape cutouts of JC elements onto the plastic domes. The STL files were instead used to print a dual colored part made up of polylactic acid (PLA) filament. The dual-colored domes were used as a guide to manually place copper-tape JC cutouts.

To account for crumpling that occurred when manually placing JC elements onto the parabolic dome, it was found necessary to update the model of the JC in the simulations. Figure 4.8 shows a comparison of the ideal element to the copper tape element after being placed on the dome. The copper tape model was generated by taking a photograph of one of the elements on the manufactured dome. The photograph was imported into MATLAB, processed, and exported as an STL. The STL of the copper tape element was imported into Ansys HFSS for simulation. Compared to the perfect element, the distorted element had noticeably rounded corners and jagged edges. The new model also accounts for JC elements that were found to be slightly elevated from the clear substrate (approximately 78 micrometers) due to the use of a dual material print. Figure 4.9 shows the infinite array simulation of a perfect JC versus the copper tape model. This simulation also accounts for a very slight difference in permittivity between the colored plastics (blue and clear with $\varepsilon_r = 2.55$ and $\varepsilon_r = 2.52$ respectively). A large frequency shift is noted between the two simulations; perfect elements exhibited a response at 10 GHz while the copper tape elements exhibited a response at 10.68 GHz.

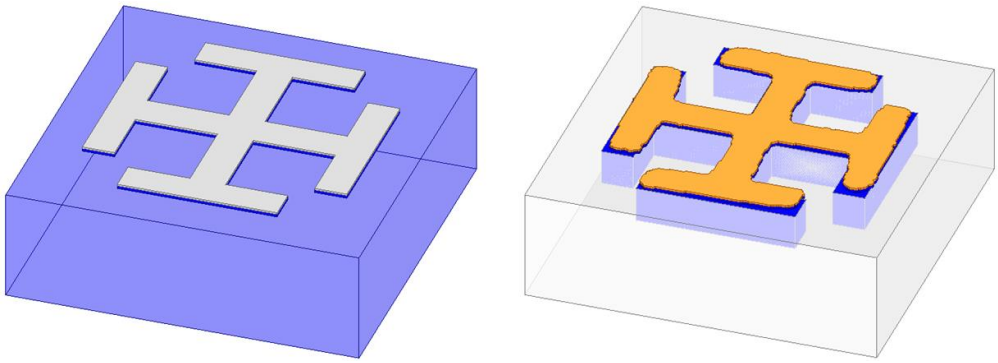

Figure 4.8 On the left is a perfect JC and on the right is a realistic model of the copper tape elements.

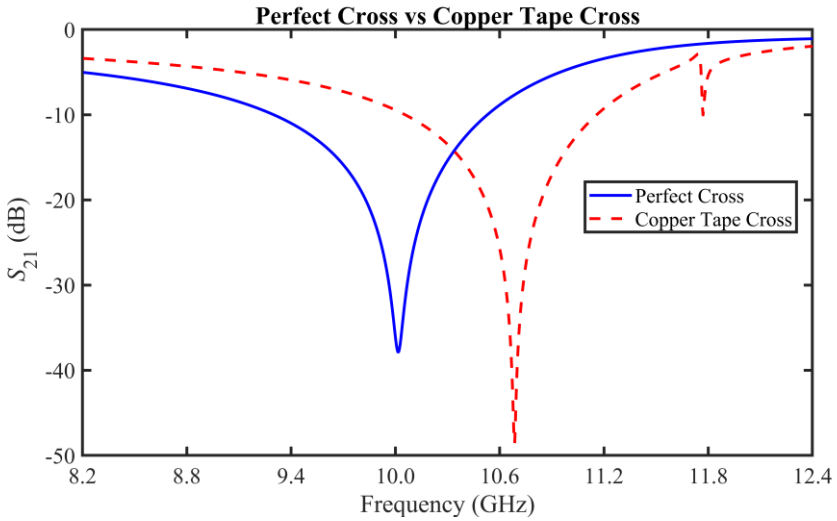

Figure 4.9 Infinite array simulations comparing the response of perfect JC (in blue solid line) versus the realistic model (shown in dashed red line). A 0.68 GHz shift in resonant frequency is observed.

4.4 Demonstration Devices

In total, three FSSs were produced. The first device was a standard, flat 10×10 array. The second device was a parabolic dome with a projected array. The third device was the same parabolic dome with an array generated by the SVL algorithm. Photographs of these devices are provided in Figure 4.10. All three domes were 3D printed using an Ultimaker3 with PLA filament. The substrates were printed using clear filament while the arrays of JC elements were printed using blue filament. All three devices were populated by hand with copper JC cutouts made using a

Cricut Maker. At the time of this work, no hybrid-direct write solution for printing these types of conformal arrays existed. In recent works, OmniSlice™ added the capability of printing conformally on virtually any surface, including steep walls, with the use of 3-axis 3D printing systems. [96]

Figure 4.10 All three assembled FSS devices. From top to bottom, flat FSS, projected FSS, and conformal SVL FSS.

4.5 Measurements and Discussion

After all models were assembled, the error in the period of the conformal SVL FSS was measured. Measurements were done by hand with the use of calipers. One set of measurements

was done for JC elements that followed the direction of the lattice vectors where the calculated period is exact. Another set of measurements was done for JC elements along a diagonal direction where error in the period is more noticeable and elements are visibly closer together. The percent error of the measured period relative to the exact period was calculated. On average, for elements that follow the direction of the lattice vectors an error of 2.01% was found. For elements along a diagonal direction, an average error of 10.22% was measured. The larger error for diagonal elements was expected of the conformal SVL algorithm due to the period being enforced along the direction of the lattice vectors used.

The free-space response of the three assembled models was measured in the EM Lab's anechoic chamber using an Agilent N5245A PNA X Vector Network Analyzer. Two ports were used and were connected to two Arra, Inc., WR90 horn antennas. A picture of the measurement setup is shown in Figure 4.11.

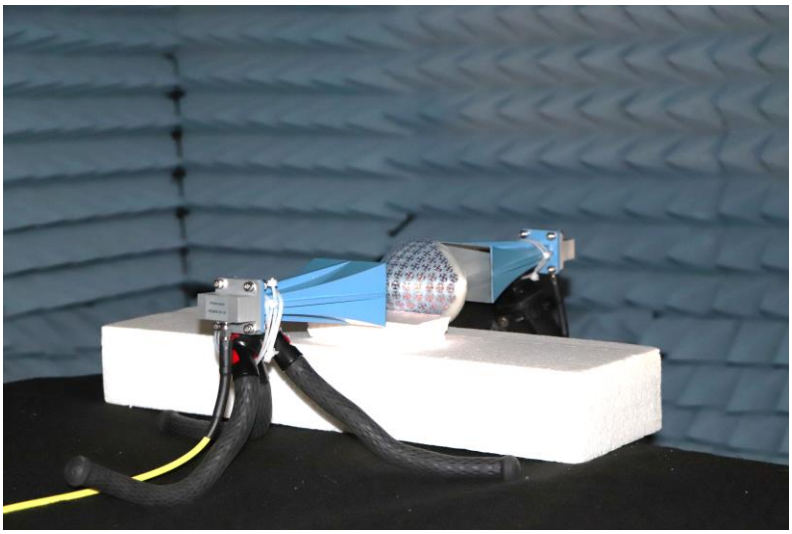

Figure 4.11 Measurement setup showing SVL FSS on a parabolic dome.

The measured results for all three FSSs are shown in Figure 4.12 along with the response from an infinite array of copper tape elements. A large shift in resonance when compared to a perfect JC cross is still observed for the assembled flat and parabolic SVL dome models. Despite

this, the conformal FSS generated by the conformal SVL algorithm is in excellent agreement with the flat FSS and infinite array simulation. As expected, the projected array did not exhibit a resonant response. This is due to the heavily distorted and stretched out elements caused by a standard projection of the array onto abrupt curvature. Contrary to that, the SVL FSS maintains periodicity without distorting the elements thus preserving the electromagnetic performance.

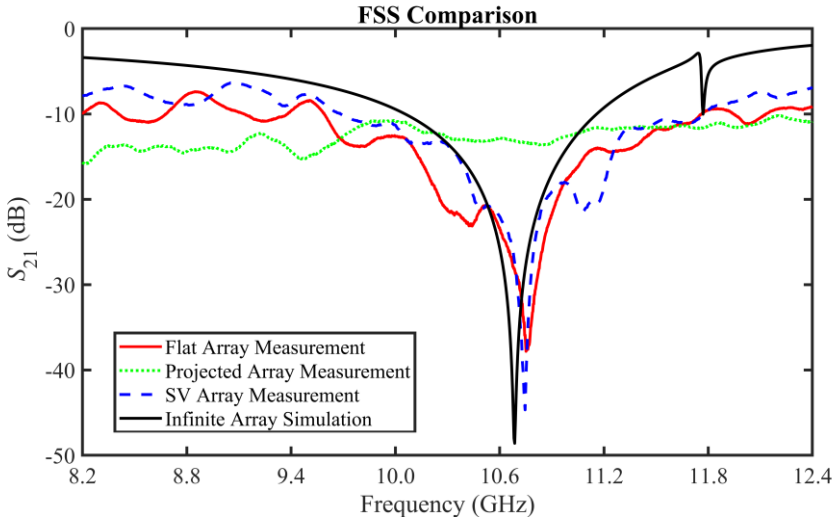

Figure 4.12 Measured results for the three manufactured surfaces.

Chapter 5: Hybrid Printed Ultrawideband Volumetric Antenna

5.1 Background on Chu Limit

First established in 1948 [83], Chu began by proposing that the entire antenna system (radiator, transmission line) be enclosed by a fictitious sphere now commonly referred to as the "Chu sphere." Within this sphere, the antenna's near field and current distribution are contained. In the far field, or outside the sphere, radiated fields are composed of orthogonal spherical modes. The total radiated power would then be sum of the radiated power contained in these modes. What happens in the far field is correlated to what happens in the near field. Chu derived his fundamental limit based on the ideal conditions that the antenna would only have a purely resistive impedance and is composed of perfect conductors with no loss. As a result, the Chu limit became the lower bound of how an antenna can operate under ideal conditions.

In real life where losses and imperfect matching is the norm, antennas are expected to at best behave close Chu limit but never capable of breaking it. From a practical perspective, the Chu limit gives antenna engineers a good idea of how an antenna can operate relative to its electrical size. There are tradeoffs between the antenna size, antenna efficiency, and bandwidth. At its limits, you can always optimize for two at a sacrifice of the third. Several other modifications to fundamental limit theory have been made in the works of McLean, Grimes, and Davis respectively [84]-[86]. Of particular interest for this work is Yang's modification to the fundamental limit theory, which ultimately led to his design of the compact ultra-wideband antenna (CUA) [87].

5.2 Compact Ultrawideband Antenna (CUA) Design

The CUA was designed by Taeyoung Yang at Virginia Tech in 2008 [88]. His design operated close to the fundamental limits established by Chu. In his dissertation, Yang offers a

good outline on how to design antennas that can perform close to the fundamental limits [87]. His design methodology for the CUA is summarized in Figure 5.1. He began by first choosing an antenna that already performed close to the fundamental limits originally designed by Best in 2004 [89]. Best's antenna model featured four helical arms sitting atop a ground plane with a feed point at the base of one of the spiral arms. A critical aspect of this design was to enhance antenna performance by designing for the entire antenna sphere as opposed to designing on a plane. This design later had its feed repositioned by Clark [90]. The contrast in Clark's design was changing the location of the feed from the base of one of the spiral arms to a center feed structure. Both helical spiral designs had narrowband operation with resonances at harmonic frequencies. Yang's design then broadened the bandwidth by adding a tapered cone as a feed connected to the top of the helixes via a wire. This wired connection yielded a frequency notch at approximately 3.6 GHz. The final model in the design's evolution featured the same tapered cone without the wired connection and, instead, was capacitively coupled to the helical antenna cage.

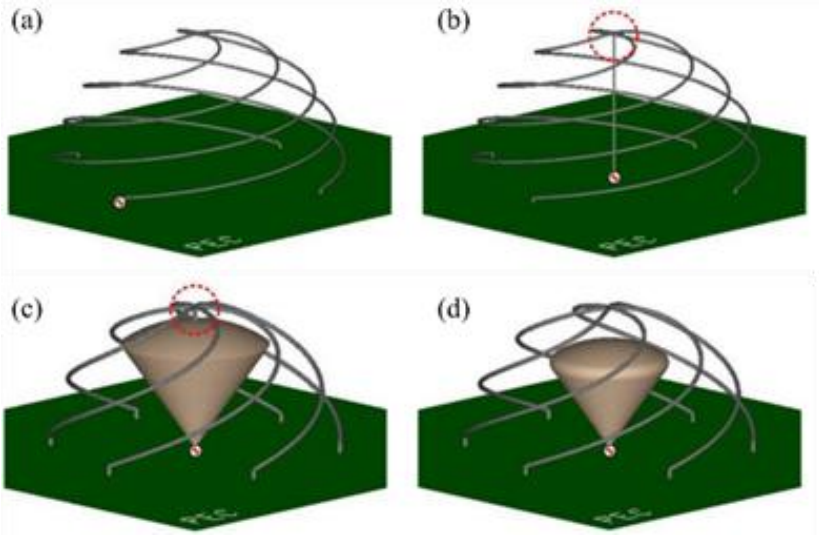

Figure 5.1 (a) Best's original folded spiral arm antenna. (b) Clark's feed modification to the spiral arm antenna. (c) Yang's addition of the tapered cone feed. (d) Yang's final CUA design with the cone feed capacitively coupled to spiral arms [87].

Yang's final design is summarized in Figure 5.2. In Cartesian coordinates, the spiral arms follow

$$\begin{bmatrix} x_a \\ y_a \\ z_a \end{bmatrix} = \begin{bmatrix} h_a \sin(\theta)\cos\phi \\ h_a \sin(\theta)\sin(\phi) \\ h_a \cos(\theta) \end{bmatrix} \tag{5.1}$$

and their angle of elevation follows

$$\theta = \cos^{-1}\left(\frac{\phi}{2\pi n}\right). \tag{5.2}$$

The angle of elevation θ spans $0 \le \theta \le \pi/2$ and the azimuthal angle ϕ spans $0 \le \phi \le 2\pi n$ where n is the total number of turns. These values are summarized in Table 5-1.

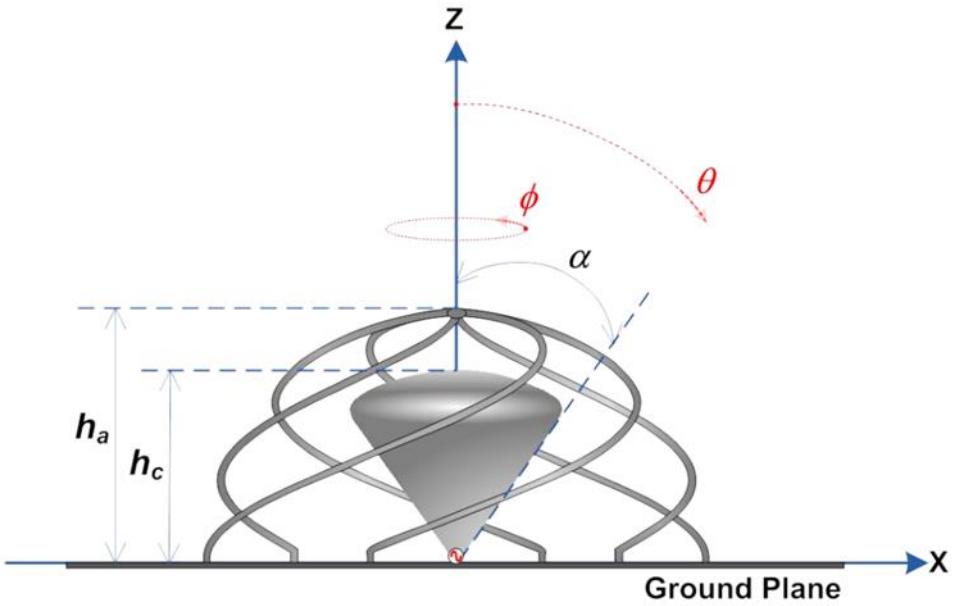

Figure 5.2 Final CUA model.[87]

Table 5-1 CUA design parameters and their respective values [87].

Antenna Design Parameter	Design Value
Overall antenna height (h_a)	15.65 mm
Feed-cone height (h_c)	12.01 mm
Feed-cone angle (α)	0.61 radian
Number of turns of each arm (n)	0.43
Wire diameter of each arm	0.50 mm

5.3 Design Motivation

While designing antennas specifically to approach the fundamental limits is not in the scope of this work, fundamental limit design has led to many interesting antenna structures. The design paradigm of the CUA was to intentionally use the entirety of the antenna sphere as a means to push its operation closer to the fundamental limits. This led to a design that fits in well with the vision of true 3D/volumetric electromagnetic design. However, there is little to no information as to how the CUA was manufactured. It can only be assumed that it was mostly made by hand. Its 3D design lends itself well to hybrid additive manufacturing approaches. This chapter describes the hybrid additive manufacturing of the CUA and the lessons learned to push the manufacturing of a functional RF structure.

5.4 CUA Modeling and Simulation

Before manufacturing began, the CUA was first characterized through modeling and simulation. All CUA simulations were carried out in Ansys HFSS. The simulated model is shown in Figure 5.3. This model features a CUA simulated in air (free floating metal). The form of excitation used was a lumped port. Lumped ports are typically used when little is known about the feeding structure that will be used for the antenna and may have a complex impedance that is defined by the user. A purely resistive impedance of 50 Ω is selected. A circular ground plane with a radius of 75 mm was used. This was in contrast to literature where modeling was typically

done on an infinite ground plane or on a ground plane with a radius of 150 mm. Through simulations, a radius of 75 mm was found to be sufficiently large to act as an infinite ground plane relative to the size of the antenna. A larger ground plane is chosen as more than sufficient. The entire simulation space is bounded by a square box with a length of 170 mm with absorbing boundary conditions enforced on its surface.

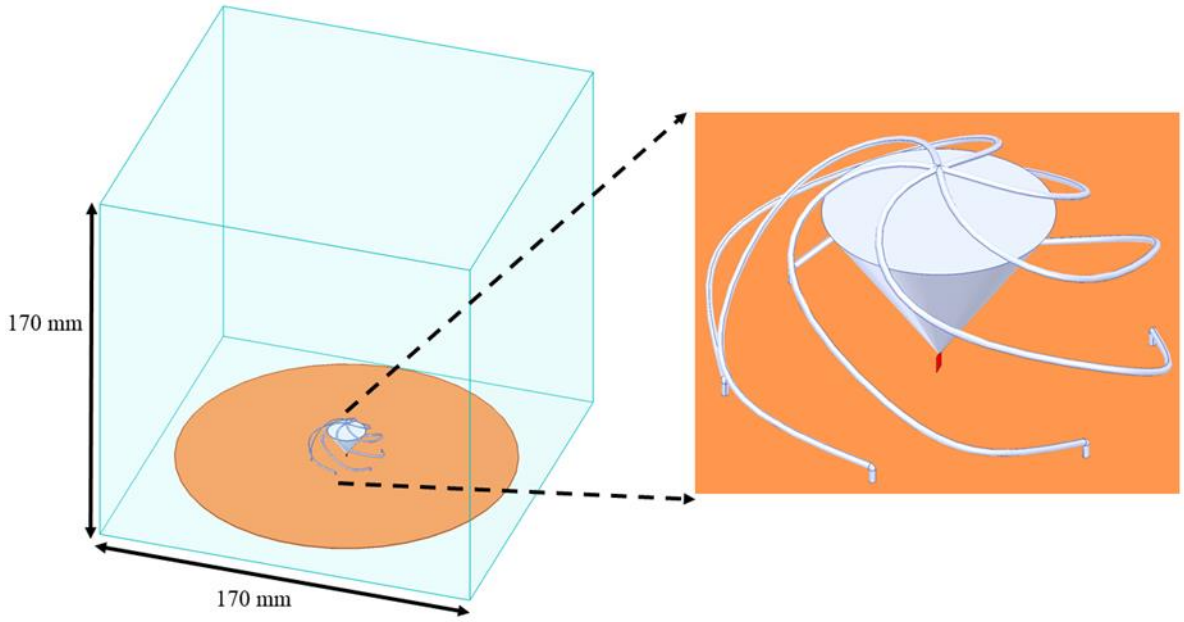

Figure 5.3 (Left) CUA model shown in air box with absorbing radiation boundaries applied at edges of simulation space. (Right) Close up image of CUA model with a lumped port shown in red.

To model the antenna structure, a single spline following (5.1) was drawn as a 3D sketch in Solidworks. This singular spiral arm path was then swept cylindrically to a trace thickness of 0.5 mm and connected to a 1 mm tall cylinder using “boundary boss/base” to ensure a connection to the ground plane. This spiral arm model was then exported from Solidworks as an IGS file and then imported into HFSS. Within HFSS, the singular spiral arm is duplicated five times. Each spiral arm is then rotated by increments of 60° about the *z*-axis. Lastly, the six spiral arms were united to form a single solid model. Alternatively, an equation based curved can also be used within HFSS. For the capacitive feeding structure, a simple cone with no rounding or

smoothing is chosen as the feed. No information is given as to the modification of the cone beyond it having a “tapered top and blended edge” [87]. For this investigation, a cone with a flat top was sufficient to characterize the CUA. Simulated results are shown in Figure 5.4. As a general rule of thumb, a voltage standing wave ratio (VSWR) of 3 or less will be targeted [91].

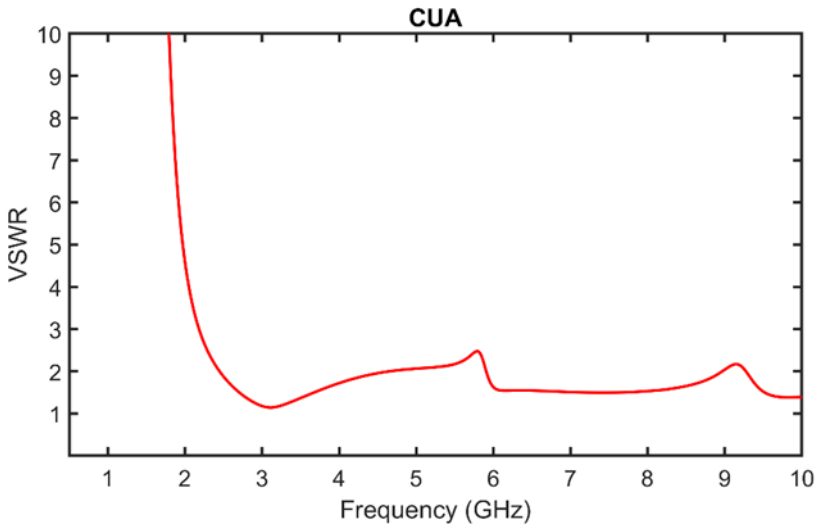

Figure 5.4 Simulated VSWR response for the CUA using a lumped port as the source.

5.5 The Gold Standard CUA

Before hybrid additive manufacturing processes can begin, two major details in the RF design must be classified. (1) Selection of the feeding mechanism and (2) ensuring no free floating/unsupported conductive traces. The “Gold Standard” design was first manufactured to select an antenna feed, assess manufacturing feasibility, and to have a good benchmark to which a hybrid additive manufactured CUA can be compared to. A secondary objective of the gold standard was to identify a proper RF measurement technique. In literature, there is no information as to what type of connector was used to feed the CUA. An assumption is made that a subminiature version A (SMA) connector was used. Although several variations of SMA connectors are commercially available, the SMA connector is generally used as the standard. An Amphenol RF 132322 connector with 50 Ω impedance and a maximum operating frequency of

18 GHz is chosen. Simulation models were updated to include an SMA connector as a feed and removing the lumped port. In its place, a waveport is used to excite the fundamental mode in the coaxial guide within the SMA model. The gold standard model with an SMA connector as a feed is shown in Figure 5.5.

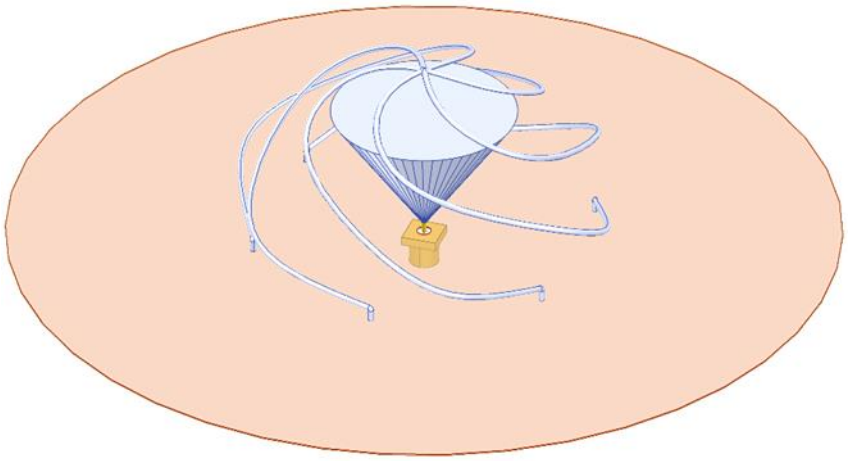

Figure 5.5 Gold standard CUA model with SMA connector as a feed.

In contrast to the original CUA model, the gold standard model was uniformly scaled by 200%. This was a necessary step in order for the model to be printed using an Ultimaker3 equipped with 400 μm pentips. The gold standard was printed in two main separate print jobs; one dual material for the spiral arms and one single material for the cone feed. The spiral arms were 3D printed using polylactic acid (PLA) fully embedded in polyvinyl alcohol (PVA) support material. A picture of the printing process is shown in Figure 5.6 (a). PVA is a water-soluble support material that allowed for the printing of the spiral arms (normally a free hanging structure) to be printed with ease. The PVA material was removed by letting the printed model sit in water for approximately 3 hours. The long duration was due to the large amount of PVA material that was printed. The spiral arms with the PVA removed are also shown in Figure 5.6 (b). Not pictured is the cone feed also printed using PLA. Supplementary PLA parts (shown in

blue PLA) were printed to hold the gold standard's feed in place and to keep the spiral arms from collapsing under their own weight.

The final step in the gold standard manufacturing is to add a layer of conductive material to the plastic parts (cone and spiral arms) that were printed. Dupont CB028 silver conductive paste is applied to the entire surface of the cone and spiral arms. This process is very typical of what is found on "3D printed antennas" in literature [92-95]. The ground plane was cut out from an 11.8 in × 8.9 in sheet of copper tape using a Cricut Maker 3. The ground plane measured 150 mm × 150 mm and contained cutouts to fit the SMA connector. The SMA connector was attached to the cone feed using conductive epoxy while the spiral arms were attached to the ground plane using Loctite superglue. The fully assembled gold standard CUA is shown in Figure 5.7.

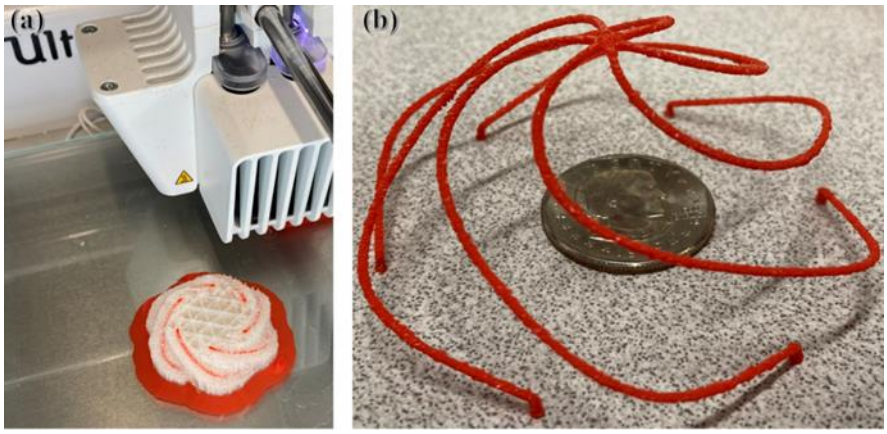

Figure 5.6 (a) Red PLA spiral arms embedded in clear PVA. (b) Spiral arms after PVA is removed.

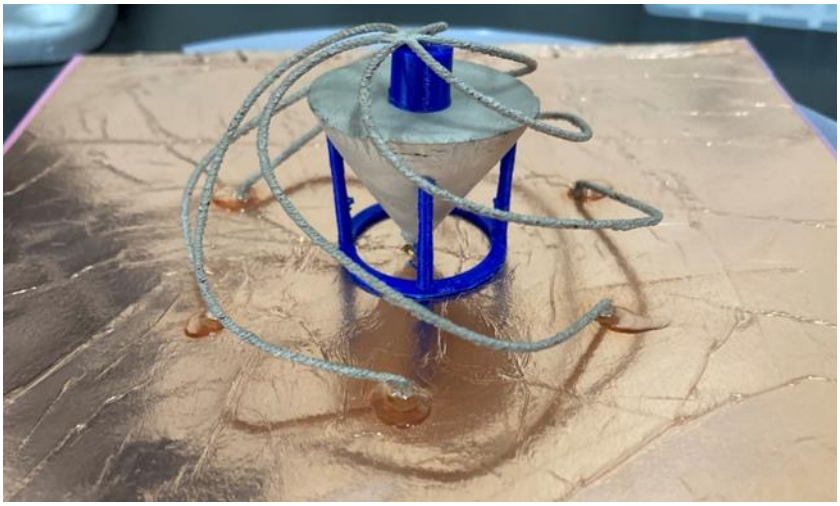

Figure 5.7 Fully assembled gold standard with blue PLA support pieces.

The gold standard was measured at the EM Lab using an Agilent N5245A PNA-X Vector Network Analyzer. The measured results are shown in Figure 5.8 in a dashed red line along with the simulated results shown in a solid red line. Both simulated and measured results stay well below the baseline of a VSWR value of 3. It can be seen that for a broader number of frequencies the measured response exhibits more power delivered to the antenna compared to what was expected from simulation.

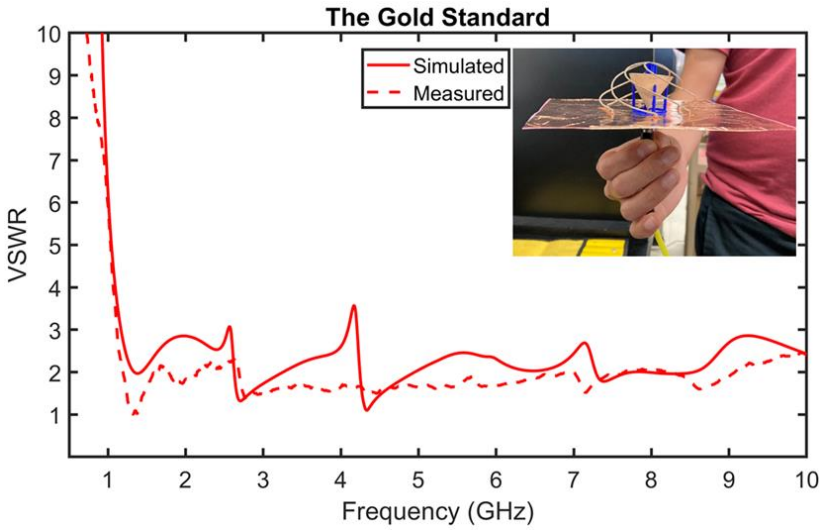

Figure 5.8 Simulated (solid red line) and measured (dashed red line) VSWR.

5.6 Preparing Models for Hybrid 3D Printing

The gold standard design answered some fundamental questions about the CUA's operation. It confirmed the selection of a feeding mechanism (SMA) as well as provided a baseline measurement to which a hybrid printed CUA can be measured up to. While it might be tempting to take the original model and "file-print," further changes to the model are needed before it is well suited for hybrid printing processes. Secondary PLA pieces were printed to support the gold standard's weight. Similarly, all conductive traces in a hybrid additive manufacturing process must be supported by a dielectric. Figure 5.9 will be used as an aid to identify key areas of the CUA design in need of support. The CUA design is made up of free-floating conductive spirals. This type of structure is incompatible with the dispensing processes of conductive pastes, particularly CB028. To approach a printable model, the original CUA design is first completely embedded within a dielectric half sphere. Similar to the holey frijole and PPTLs, completely embedding the antenna structure in ABS will ensure all traces are supported assuming an infill of 100% is used.

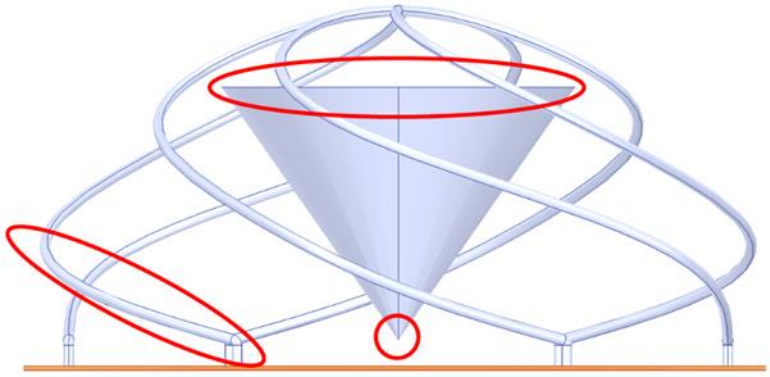

Figure 5.9 Original CUA model with problem areas circled in red.

Unlike earlier hybrid prints, embedding any singular design in a dielectric does not immediately generate a printable model. The next step towards a printable model is to ensure a minimum trace thickness and width. The initial CUA models assume that all conductors (PEC

materials) are completely solid. Specifically, the cone feed for the CUA, is assumed to be a large solid piece of conductive material. CB028, however, is a thin film conductive paste whose performance degrades the thicker and more volumetric a printed trace (or shape) is. Therefore, the next step is to generate a model of the cone feed with a hollowed out interior and a finite thickness all around. This is done by creating a scaled copy of the original cone model (scaled down to 98% its original size in this example), centering it within the original cone's volume, and subtracting it from the original model. This yields an outline of the original model with a finite thickness. The inner or hollow region is then filled with ABS. This will ensure that the top part of the cone feed will be supported by a dielectric. Figure 5.10 shows a comparison between the original model versus a printable model. A green volume is added to the inside of the cone to highlight a region that should be printed using ABS. Assigning ABS to the inside of the cone structure will give the conductor a finite thickness. In general, large conductor volumes should be avoided and their finite thickness will be solely dependent on the printing parameters chosen. It is very common to adjust these thicknesses as necessary. Particularly if different pentip sizes are used. The key printing parameters are linewidth and layer height. These two values are heavily dependent on the pentip size chosen for any particular system.

Lastly, sharp pointed structures are also not possible to be resolved in a hybrid printing process. The CUA's cone feed tapers down to a single point and must be "blunted" before it is feasible to 3D print. For this design, the CUA feed is subtracted with the SMA pin (0.7 mm in diameter). This has the added benefit of creating a hole where the inner ABS filling of the cone feed can connect to the outer ABS material. This will create a small ABS pillar that will serve as a support for the ABS inner cone.

After these modifications were done, the modified printable CUA model's performance was confirmed via simulated radiation patterns. The printable CUA's radiation patterns at various frequency points are shown in Figure 5.11. It can be seen that the printable CUA's radiation pattern remains relatively consistent at all these frequencies. The patterns are also omnidirectional and match what is seen in the source material [87]. After this confirmation, manufacturing of the CUA began.

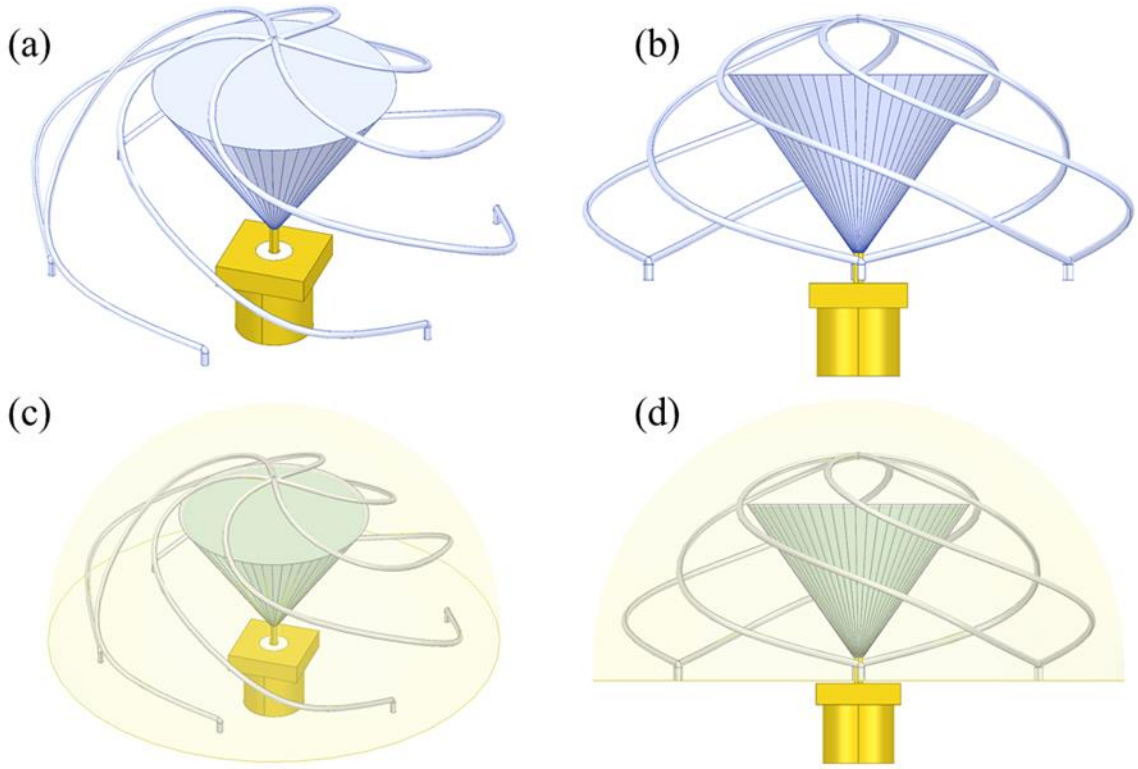

Figure 5.10 (a) Isometric view of basic CUA model with SMA feed. (b) Front view of basic CUA model. (c) Isometric view of printable CUA model embedded in ABS with inner ABS cone highlighted in green. (d) Front view of printable CUA model.

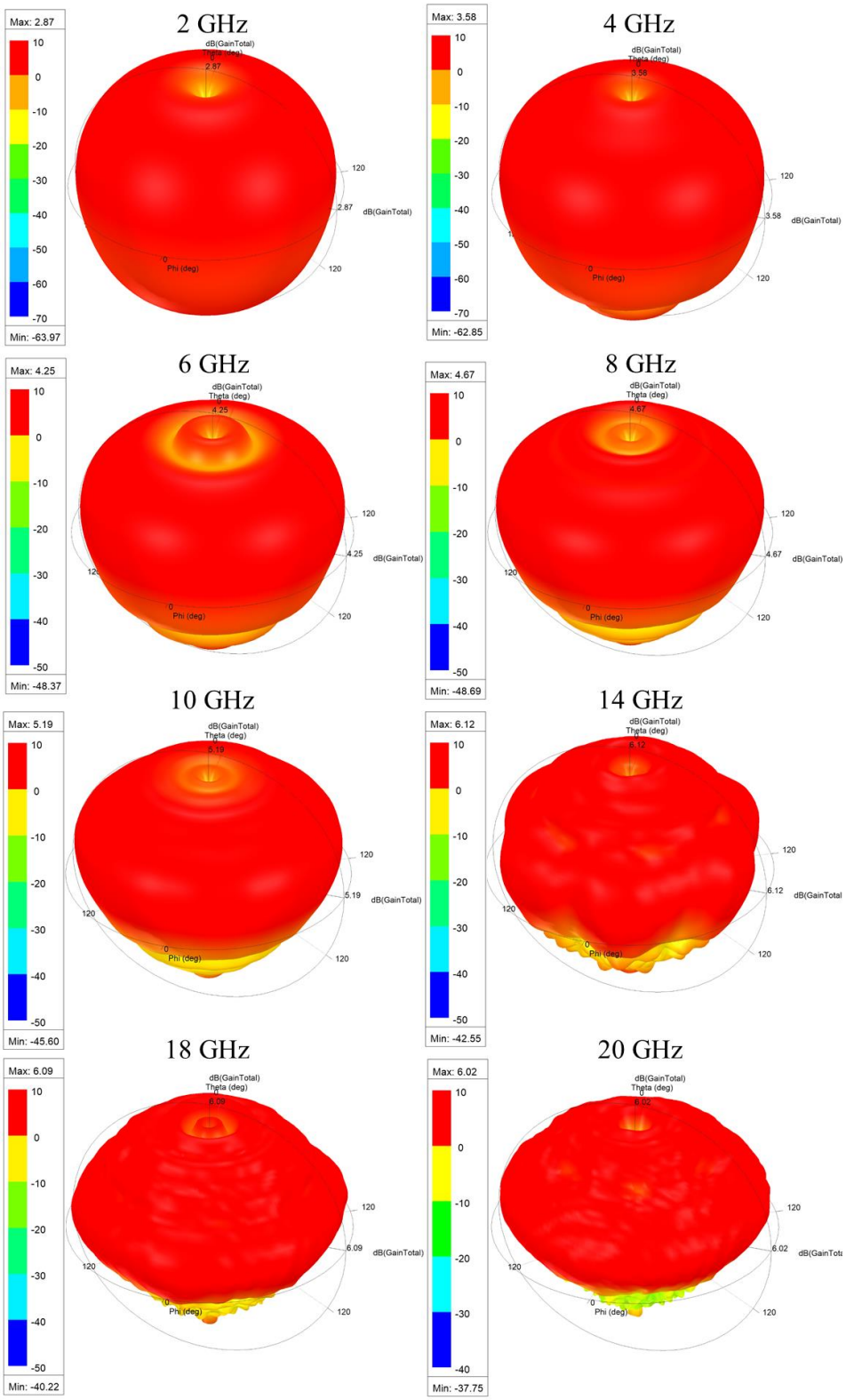

Figure 5.11 3D simulated radiation patterns for the printable CUA model at various points in frequency.

5.7 HYBRID 3D PRINTING OF 2.5D CUA

Initially, CUA printing attempts were done using Tabletop #1 with the same parameters originally used for the holey frijole and PPTLs (Table 3-2). One of the biggest issues faced during this process was the long print time. An entire hybrid printed CUA process was taking beyond 16 hours, often failing near the 12 hour mark. Additionally, Tabletop #1's nFD™ and Smartpump™ toolheads were in very close proximity to each other. This led to a high thermal cross talk between both tools and premature drying of CB028 within the Smartpump™'s pentip. Coupled with the long print duration yield was extremely low. Two scenarios often played out. The ink would either completely stop flowing or would slowly lose flow as the hybrid printing process would continue. This was more clearly observed through x-ray imaging of CUA prints shown in Figure 5.12. Figure 5.12(a) shows a scenario where the conductive paste flow abruptly stops presumably due to a pentip clog due to a messy print process and premature drying of paste in the Smartpump™'s pentip. Figure 5.12 (b) shows a more gradual decrease of conductive paste flow. More material is dispensed during the first printed layers and the flow gradually decreases as the print job is completed.

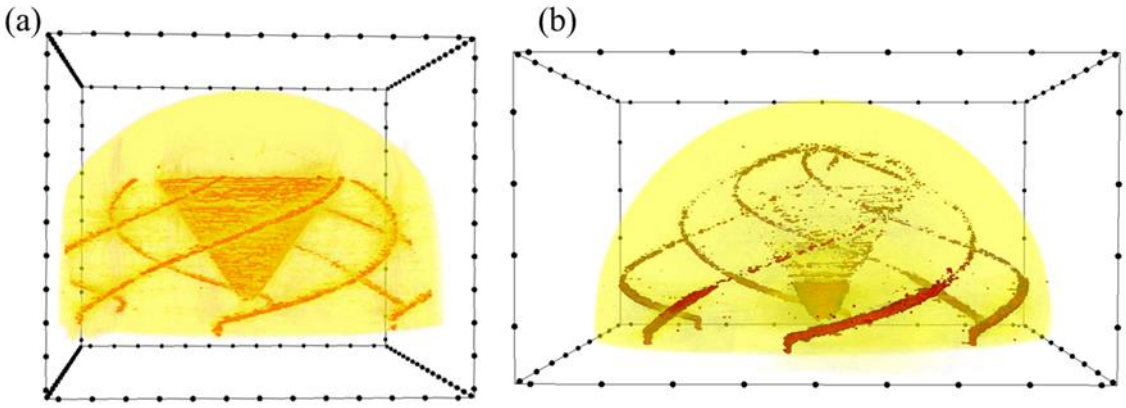

Figure 5.12 (a) X-ray image of CUA showing abrupt stop in conductive paste flow. (b) X-ray image of CUA showing a more gradual decrease in conductive paste flow as print job continued.

To account for these issues, the first true hybrid volumetric print of the CUA was printed via a 2.5D approach. All proceeding hybrid prints were moved to Tabletop #2. Although lacking in tools by comparison, the added slots allowed for the use of the nFD™ in the slot opposite and furthest from the Smartpump™. This eliminated the thermal cross talk issues experienced with Tabletop #1. The CUA was broken up into six separate segments with varying thicknesses. These segments and their respective thicknesses are shown in Figure 5.13. Each segment was manufactured individually each as a hybrid print job. A CUA would then assembled by aligning and stacking all six pieces in order. This emulates the 2.5D PCB stacking approach commonly found in literature.

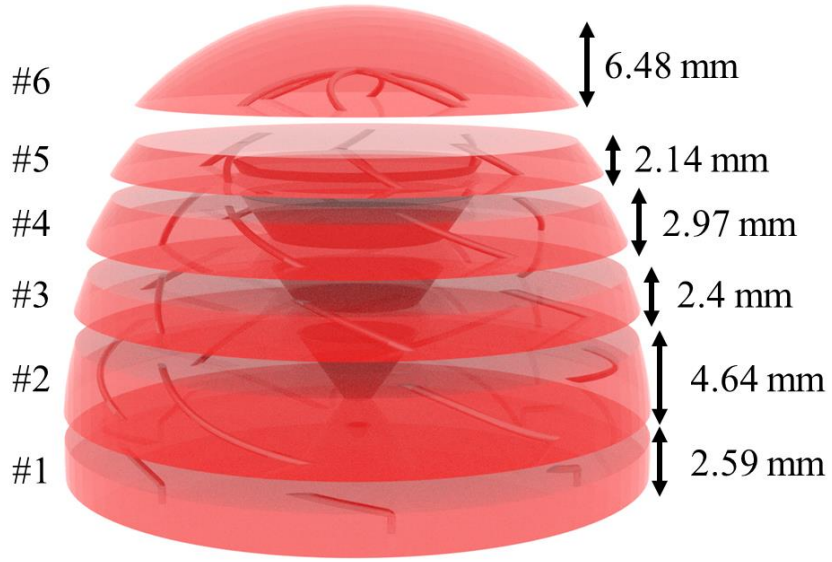

Figure 5.13 CUA model showing all 6 segments and their respective thicknesses. This model will be used to fabricate a CUA using a 2.5D approach.

All six segments were printed using the updated printing parameters in Table 5-2 in combination with OmniSlice™. While OmniSlice™ is not limited to the parameters listed, these were chosen as the most critical. Stark differences between the original printing parameters (Table 3-2) are observed. Firstly, this was the first time printing with a mismatched set of pentips. The Smartpump™ pentip was swapped to a smaller (100 µm) diameter. This caused an

overall decrease in flow allowing for more even filling of cavities with the conductive paste. The layer height was increased by 50 µm to decrease overall print duration. Likewise, the linewidth was decreased to account for the increase in layer height. This new value of linewidth is still very capable of resolving the smallest feature in our model (0.5mm – spiral arm diameter). Retraction distance was slightly decreased to minimize filament grind. The biggest changes pertained to the Smartpump™ parameters. To account for the overall decrease in flow of conductive paste due to a smaller pentip diameter, the Smartpump™'s movement speed was decreased by 5 mm/s. Perhaps the biggest change here is with regards to the valve delta. The delta was largely increased from 42 µm to 175 µm. The design philosophy was to control the flow of conductive paste solely through the use of print speed and pressure rather than through a finely tuned delta. The larger valve delta also decreased the frequency of pentip clogs since it allows conductive paste to more readily flow. Pressure was adjusted accordingly throughout the printing processes for all CUA segments increasing/decreasing the flow as was seen necessary ranging from 4-6 PSI. The dispense gap was only slightly increased to account for the 100 µm pentip naturally seating slightly lower in comparison to a 125 µm pentip. It is noted here once again that the "dispense gap" value accounts for both layer height, toolhead delta, and the true dispense gap.

Table 5-2 Slicing parameters used as an input for OmniSlice™ for 2.5D CUA hybrid prints.

Parameter	nFD™	Smartpump™
Pentip diameter	125 µm	100 µm
Layer height	0.100 mm	0.100 mm
Linewidth	0.150 mm	0.150 mm
Perimeters	1	1
Infill	100%	100%
Speed	40 mm/s	10 mm/s
Top layer count	0	0
Bottom layer count	0	0
Extrusion factor	0.9	N/A
Retraction distance	3	N/A
Retraction speed	10	N/A
Valve open/close Speed	N/A	1.0 mm/s
Valve delta	N/A	0.175 mm
Pressure	N/A	4-6 PSI
Dispense gap	N/A	0.200 mm*

Figure 5.14 shows segment #3 during printing as well as all the segments printed. The combination of all these parameters led to hybrid prints that were majorly improved. The larger valve delta allowed for a more consistent conductive paste flow. The reduction in thermal crosstalk reduced the number of clogged pentips caused by the drying of the conductive paste in the Smartpump™ pentip. Both of these changes combined yielded consistent hybrid prints for a longer duration. Table 5-3 shows the overall print time for each of the six segments. The overall print time was reduced to 14.34 hours for all segments. Although only a minor reduction in overall print time, the lower print time per segment allowed for more rapid prototyping. The seam along the side of the segments was used to align all pieces for assembly. A small hole was drilled in first segment to connect the SMA to the embedded cone feed. Clamps were used to apply pressure on all the segments and ensure that all segments made contact with each other. Similar to the gold standard, a ground plane was fashioned out of copper tape made using a Cricut Maker 3.

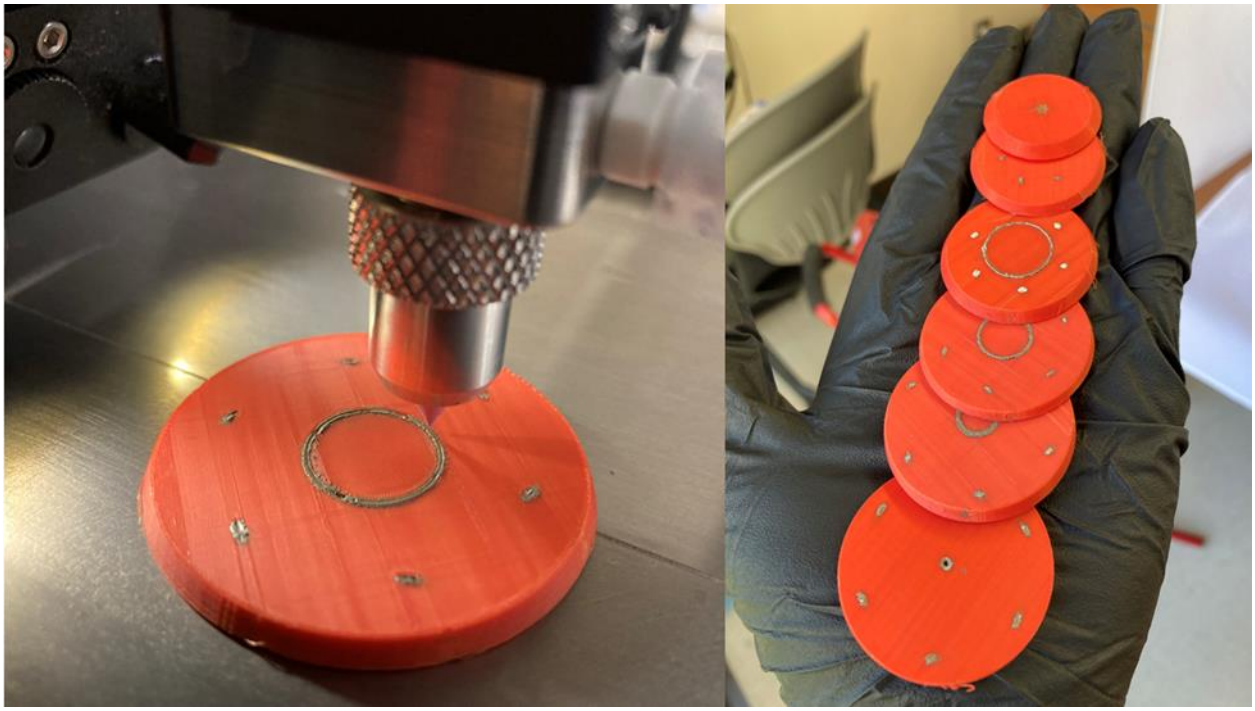

Figure 5.14 (Left) 2.5D CUA segment #3 with more consistent conductive paste flow. (Right) All printed 2.5D CUA segments.

Table 5-3 2.5D CUA segment print durations.

Segment #	Print Duration
1	2.3 hours
2	4.15 hours
3	2.14 hours
4	2.32 hours
5	1.5 hours
6	1.93 hours

The 2.5D CUA was measured at the EM Lab using an Agilent N5245A PNA-X Vector Network Analyzer. Figure 5.15 shows the 2.5D CUA's response along with the response of the gold standard. The 2.5D approach failed to yield a response to the level of the gold standard. However, the 2.5D CUA was able to maintain a VSWR level below 3. The degraded response can be explained due to any potential alignment issues during assembly. The 2.5D CUA, including the SMA connector and ground plane, will have a total of 41 contact points. Any

misalignment of these contact points will overall degrade the response of the device. This is a common problem with 2.5D approaches where alignment tolerances must be very tight.

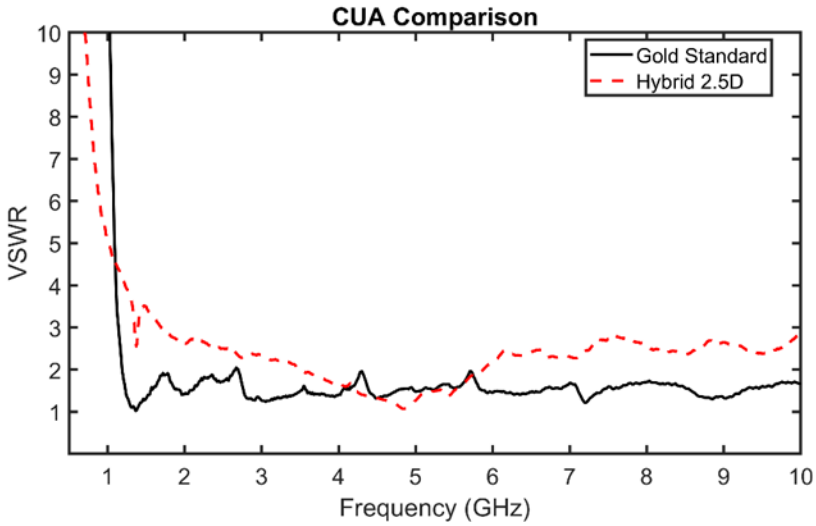

Figure 5.15 Measured VSWR results for the 2.5D CUA compared to the gold standard.

5.8 Hybrid 3D Printing of Monolithic CUA

The 2.5D CUA provided results with an acceptable response of VSWR below 3.0. However, it failed to live up to the gold standard. It was clear that to achieve a better response and overall higher yield two things needed to be done; (1) a fully monolithic CUA design should be printed in a single print job and (2) print time would need to be reduced significantly to increase the number of print iterations. To decrease overall print time, the pentip used for the nFD™ toolhead was changed to a custom sized 400 µm and the Smartpump™ was outfitted with a 200 µm pentip. To account for these changes all printing parameters were tuned to the values shown in Table 5-4.

With a much larger inner diameter on the nFD™ toolhead, layer height was increased to 200 µm. Layer height for the Smartpump™ was matched. Although OmniSlice™ accepts a different value for each toolhead, it is recommended to keep layer height the same for all tools regardless of the pentip chosen to avoid disordered layers/toolpaths. Linewidth for the nFD™

was increased to 0.480 mm. At this size, it was necessary to update the original CUA model whose smallest feature size at 0.5 mm cannot be accurately resolved with a linewidth this large. Figure 5.16 shows an updated model with the increased conductor thicknesses as well as a front view of the updated cone feed. The diameter of the spiral arms was increased to 1 mm. The thickness of the cone feed was increased to 0.4 mm. As a result, the cone feed was "blunted" further to ensure the ABS material inside the cone feed would be properly supported. Further, four cutouts were made that would add more support for the structure. Although the value of the conductor thickness is smaller than the linewidth for the nFD™ it is large enough to leave a cavity that can easily be resolved by the linewidth of the Smartpump™ at 0.1 mm. The linewidth of the Smartpump™ is not equivalent to the thickness of the trace to be dispensed. Assuming 100% infill at these values the Smartpump™ will have 4 passes within an nFD™ cavity with a diameter equal to 0.4 mm. For this reason, the Smartpump™ perimeters were decreased to 1 and its infill decreased to 0%. With these parameters the Smartpump™ will be limited to 1 pass along the perimeter of each cavity. In turn this allowed for more even dispensing in the monolithic CUA as shown in Figure 5.17.

Table 5-4 Final slicing parameters used to hybrid print monolithic CUA.

Parameter	nFD™	Smartpump™
Pentip diameter	400 µm	200 µm
Layer height	0.200 mm	0.200 mm
Linewidth	0.480 mm	0.100 mm
Perimeters	2	1
Infill	50%	0%
Speed	40 mm/s	10 mm/s
Top layer count	45	24
Bottom layer count	5	0
Top/bottom layer infill	100%	25%
Extrusion factor	0.9	N/A
Retraction distance	1	N/A
Retraction speed	4	N/A
Valve open/close Speed	N/A	1.0 mm/s
Valve delta	N/A	0.175 mm
Pressure	N/A	4-15 PSI
Dispense gap	N/A	0.040 mm

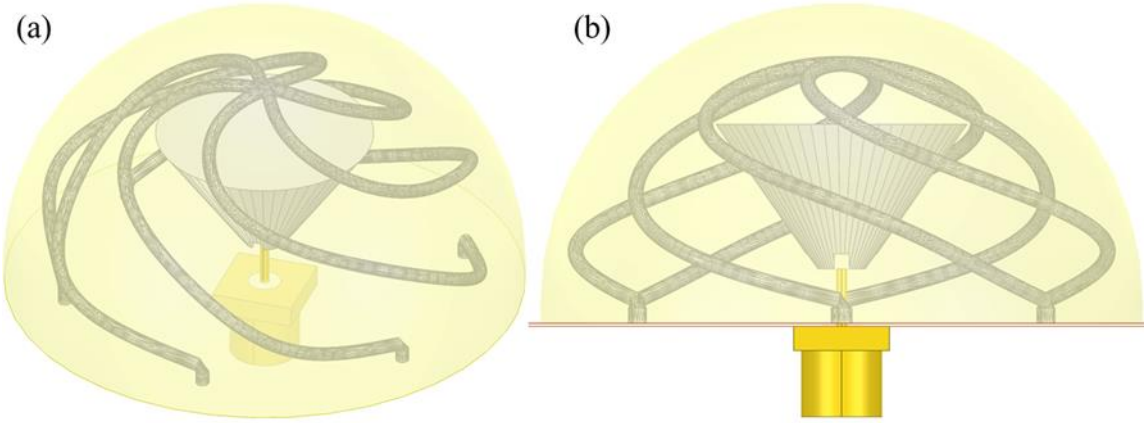

Figure 5.16 (a) Isometric view of updated CUA model with thicker conductive traces. (b) Front view of monolithic CUA model.

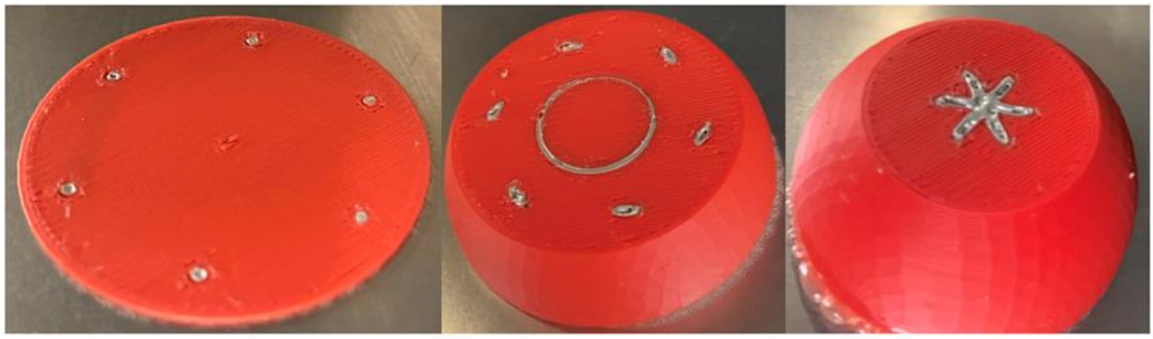

Figure 5.17 (Left) Monolithic CUA during beginning stages of hybrid print, (middle) during middle stages of hybrid print, and (right) during final stages of print. Cleaner printing process was achieved with updated slicing parameters.

Perimeters for the nFD™ were increased to 2. As a best practice, this value should be at minimum two or three. This will allow for cavities to be sufficiently defined while minimizing any potential gaps (where conductive paste can seep through). Infill for the nFD™ was reduced to 50% as a means to decrease print time. Instead, any necessary solid layers are controlled through the top/bottom layer count value. For the nFD™, 45 top layers are selected. This will ensure 5 solid layers of ABS will be printed before the flat top of the cone feed is dispensed. A new best practice was found here. At a minimum, material interfaces must be supported by four solid plastic layers (top and bottom). During this work, OmniSlice™ was not capable of automatically detecting material interfaces thus the need to manually choose these values using top/bottom layer count. Likewise, the flat top of the cone feed must be printed at an infill value of 25%. This is a change from printing all solid conductive paste layers at 100%. Depending on Smartpump™ linewidth, 100% is not always necessary and may lead to an excessive amount of conductive paste dispensed. Such was the case here where Figure 5.18 shows the difference between solid ink layers printed at 100% versus 25% infill. In the case for 100% infill, uneven amount of conductive paste can be seen with very large pools in certain areas. In comparison to

25% infill where it can be seen that the conductive paste is more evenly and cleanly dispensed over the top of the cone feed.

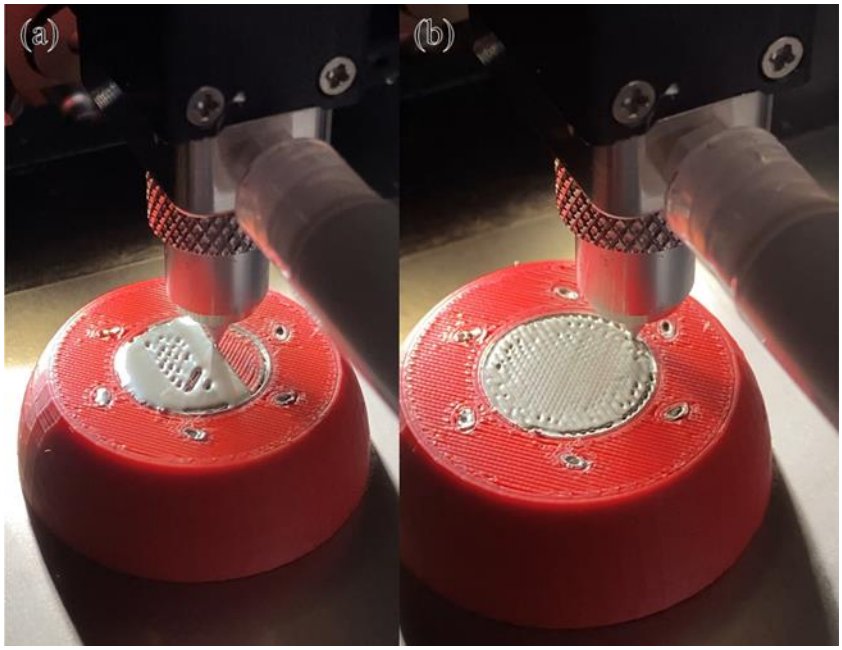

Figure 5.18 (a) Top of cone feed printing with 100% Smartpump™ infill showing large pooling of conductive paste. (b) Top of cone feed printing with 25% Smartpump™ infill showing a much more even dispensing of conductive paste.

At a layer height of 200 µm and a conductor thickness of 400 µm, a total of two ink layers will be dispensed for the top part of the cone feed. To avoid this, the cone model's top layer is reduced by 200 µm so that only a single layer is dispensed. The cavity itself is left at 400 µm to avoid any smearing of the conductive paste when the ABS plastic layers are printed thus accounting for any slight overflow of the conductive paste. Figure 5.19 shows the top of the cone feed covered by one, two, and then lastly five plastic layers relative to the final layer of conductive paste for the cone feed. For the first two solid layers, the ABS appears under-extruded and gaps can be seen. After a fifth layer of ABS, the top of the cone feed is completely covered and could once again potentially support a conductive layer. Throughout the printing process, the flow of the ink was tuned as was seen necessary by changing pressure ranging from

4 to 15 PSI. It is also noted here that improvements to OmniSlice™ were made in regards to the dispense gap whose value was set to 0.040 mm. The value used is a true dispense gap ensuring that ink was always deposited at 0.040 mm above the previously deposited plastic layer. This was a welcomed user-friendly change.

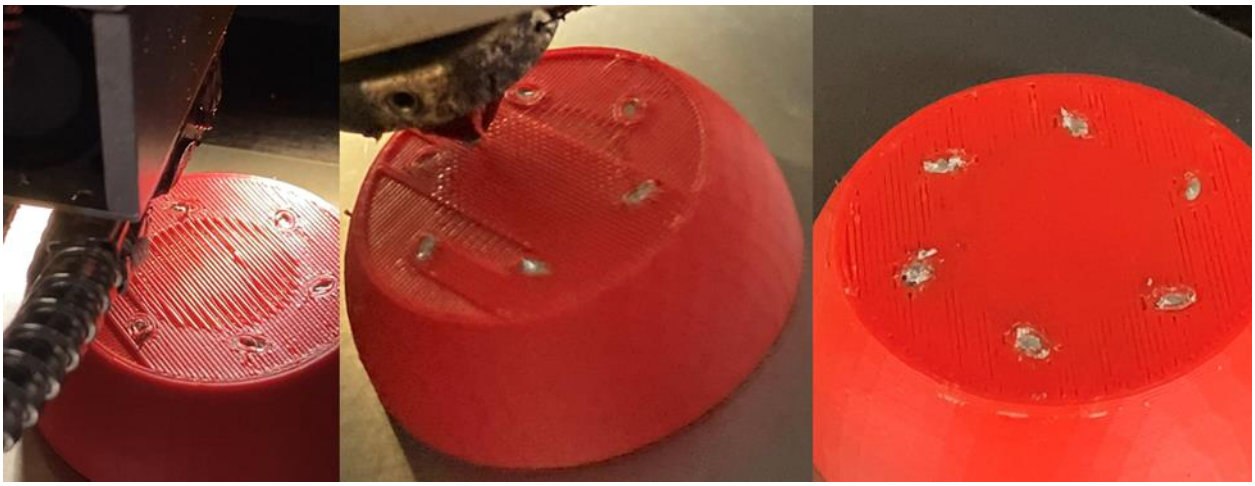

Figure 5.19 (Left) Top of CUA feed covered by a single plastic layer, (middle) two plastic layers, and (right) with five plastic layers.

Overall, the print time for a full sized monolithic CUA was decreased to 3.97 hours. The improved print time allowed for more tuning of printing parameters through increased print iterations. A total of five monolithic CUAs were able to be printed before having to refill the syringe with conductive paste. To measure the monolithic CUA, a deeper hole had to be drilled in order to fit the SMA connector. To improve electrical contact, a layer of CB028 was added to the cavity. This was the only instance where a subtractive process was used. The same ground plane used to test the 2.5D CUA was used to seat the monolithic CUA. An Amphenol RF 132322 connector with 50 Ω impedance was also used. The monolithic CUA was measured at the EM Lab using an Agilent N5245A PNA-X Vector Network Analyzer. The measured results are shown in Figure 5.20 against measured results for both the 2.5D CUA and the gold standard.

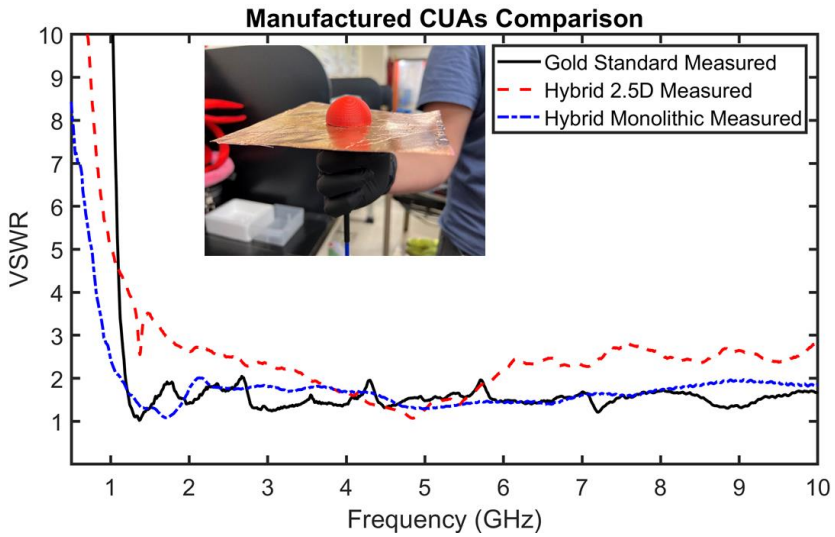

Figure 5.20 Measured VSWR for all manufactured CUAs compared to the gold standard.

In general, a shift in the frequency response can be observed in the printed models when compared to the CUA simulated in air. This is due to multiple reasons. For the gold standard, the model was uniformly scaled by 200% making the overall antenna geometry larger. For the hybrid printed CUAs (both 2.5D and monolithic), both models were fully embedded in ABS plastic. Embedding an antenna in a dielectric has the effect of loading the antenna making it appear electrically longer, thus a shift in frequency is observed. The loading effect can be minimized by printing at an infill below 100%. Although the hybrid 2.5D CUA met the metric for a broadband antenna with a VSWR below 3, it failed to operate better or close to the gold standard (except for a small range of frequencies near 5 GHz). This can be explained due to the large number of contact points and poor alignment tolerances. This drawback observed when 2.5D printing was overcome by printing a monolithic design in a single hybrid print job. In contrast, the hybrid monolithic CUA performs much better and maintains a VSWR below 2. For certain frequency ranges, the monolithic CUA performs better than the gold standard all while being half the overall size.

5.9 Summary of Best Practices and Design Rules

Throughout this work, best practices for hybrid printing were developed. In general, pentips (or nozzle sizes) were selected based on the feature sizes of the device to be printed. Larger pentips imply shorter print times (rapid prototyping) at the expense of being capable of resolving finer feature sizes. After pentips are chosen, calibration is the next critical step. Calibration entails finding the position of each toolhead at a common point in order to calculate the difference in *x*-, *y*-, *z*-positions for each toolhead. This will allow the slicer to generate accurate toolpaths with an accurate dispense gap. Another critical best practice found was to thermally isolate thermoplastic extruding heads from dispensing heads containing conductive pastes. This step is particularly crucial for prints with long durations and keeps the conductive pastes from drying by being in close proximity to extruding heads commonly operating at 200-250°C.

Design rules were drawn from the printing parameters themselves. These design rules were explored through the hybrid printing of a compact ultrawideband antenna (CUA) but are applicable for the hybrid printing of arbitrary metal/dielectric arrangements in general. As discussed, printing parameters are directly tied to pentip selection. Assuming best practices are followed, design rules can be summarized as follows:

- Smallest model feature size should be on the order of 1-2 thermoplastic linewidths
- Thermoplastic perimeters should be at minimum 2-3
- For small conductor areas, conductive paste paths should be kept to 1-2 perimeters at 0% infill
- For large conductor areas, conductive paste paths should vary in infill from 25%-50%

- Material interfaces (dielectric - metal - dielectric) should be kept to 5 solid dielectric (or thermoplastic) layers above and below an interface
- Material interfaces should be kept within 2-3 thermoplastic linewidths to avoid shorts
- Pressure for conductor dispensing heads should be varied throughout the print accordingly

While the slicing solution used (Omnislice™) was capable of detecting material interfaces between different toolheads, it did not have a feature to automatically assign 100% dielectric infill at these layers in order to physically support the conductive paste dispensed in those areas. For this work, it was simple enough to assign solid infill via the use of top/bottom layer counts. The top/bottom layers were hardcoded to directly correlate with the top and bottom of the CUA model itself. This was why a large number of top layers was used to ensure that the flat top of the CUA's conductive cone feed would be supported by 100% dielectric infill. The CUA model contained only a single material interface that required support making this approach feasible.

A trend was observed where in order to minimize print duration, a larger pentip needed to be used for the thermoplastic extruder. This led to larger linewidths that were incapable of resolving small feature sizes. Therefore an important balance between rapid prototyping (short print duration) and high resolution (long print duration) is left to the user. Alternatively, models can be printed with larger nozzle diameters at quicker iterations to prove initial concepts at the cost of large feature sizes. As a final step, a model with high resolution, albeit at a longer print duration, can be printed as the final device.

Chapter 6: Conclusion and Future Work

6.1 Summary of Contributions

In this work two main contributions that enabled the push of electromagnetics to the third dimension were achieved. Firstly, an algorithm capable of generating FSSs that conform to any shape, curvature, or surface was presented in Chapter 2. This algorithm can be applied to any element and even slot arrays. In Chapter 4, the algorithm was demonstrated using a JC array conformed to extreme curvature while still maintaining the performance of the array. Secondly, 3D/volumetric hybrid additive manufacturing processes were pioneered via the 3D printing of wearable electronics, the world's first 3D/volumetric circuit, RF interconnects, and lastly a volumetric antenna design. To the author's knowledge, this is the first hybrid 3D printed ultrawideband antenna with a 3D/volumetric design. Printing parameters as well as design rules and best practices are presented in Chapters 3 and 5. These design rules and best practices can be applied to any arbitrary arrangement of metals and dielectrics in 3D space.

6.2 Future Work

The conformal SVL algorithm presented in this work is not limited to any curve or element. As an example, different elements on different surfaces are shown in Figure 6.1. A hexagonal array of triangular loops conformed to a large random surface is shown on the top while an array of JC elements was conformed to the wing of a UAV on the bottom. These are but a few examples of the algorithm's capabilities. The flexibility of this algorithm will allow for the investigation of FSSs (or any periodic structure) that can be placed on any curvature regardless of constraints such as bend radius, large slopes, etc. Furthermore, the algorithm outputs STL files making it suitable for 3D printing approaches. Ideally, conformal FSS could be printed using hybrid 3D printing approaches with one file describing the FSS array elements (conductive) and

another describing the curvature (PLA or other thermoplastics). 3D printing systems that make use of more than three axes are well suited for conformal hybrid printing approaches. For standard hybrid printing systems, novel conformal printing approaches can be investigated. Off axis slicing, hybrid off axis toolpath planning and printing, among others can be explored.

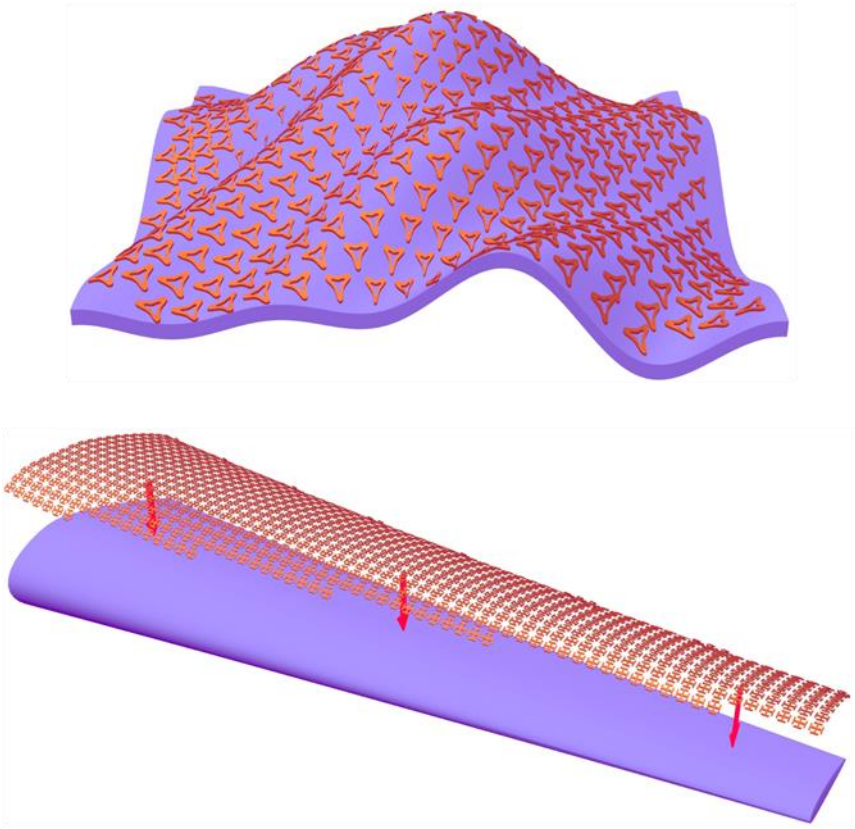

Figure 6.1 (Top) Triangular loop elements with hexagonal symmetry arranged over large random curvature. (Bottom) JC elements conformed to UAV wing.

For hybrid 3D printed circuit and antenna applications, any arbitrary distribution of metal and dielectrics can now be printed. This will allow for novel antenna designs that can benefit from designing specifically for the third dimension. In addition, designs that enable the use of multiple materials can be explored. ABS plastic, Preperm ABS1000, and conductive paste are a few of the examples shown in this work. A mockup 3D/volumetric circuit with alternating layers of materials is shown in Figure 6.2. Designs such as these can be printed with the use of

commercially available slicing software OmniSlice™. With this slicing solution, a virtually unlimited number of toolpaths can be generated each assigned to multiple materials. Metamaterials that make use of multiple dielectric constants or gradients can be explored. The design of volumetric antennas in combination with metamaterials can drive a new field of antenna design that could perhaps beat the fundamental Chu limit.

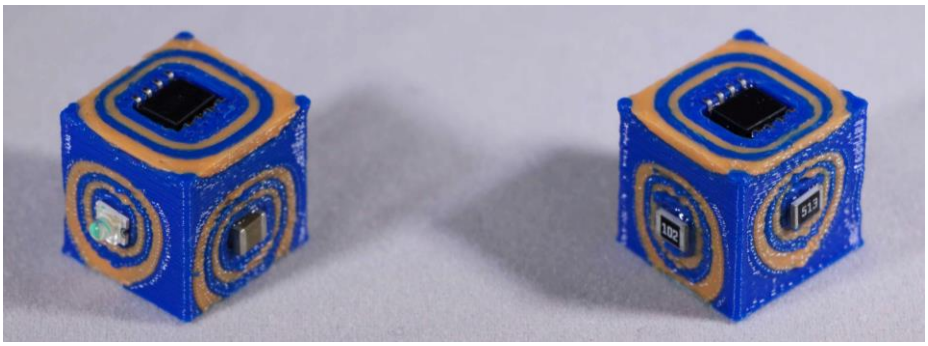

Figure 6.2 3D circuit mockup with multi-material alternating layers.

References

1. Crump, S. Scott. "Apparatus and method for creating three-dimensional objects." U.S. Patent No. 5,121,329. 9 Jun. 1992.
2. Crump, S. Scott. "Modeling apparatus for three-dimensional objects." U.S. Patent No. 5,340,433. 23 Aug. 1994.
3. Batchelder, John Samuel, and Steven Scott Crump. "Method for rapid prototyping of solid models." U.S. Patent No. 5,866,058. 2 Feb. 1999.
4. Crump, S. Scott, et al. "Process of support removal for fused deposition modeling." U.S. Patent No. 5,503,785. 2 Apr. 1996.
5. Xie, Yangbo, et al. "Microwave metamaterials made by fused deposition 3D printing of a highly conductive copper-based filament." Applied Physics Letters 110.18 (2017): 181903.
6. Miller, W. Doyle, David M. Keicher, and Marcelino Essien. "Precision spray processes for direct write electronic components." U.S. Patent No. 6,251,488. 26 Jun. 2001.
7. Deffenbaugh, Paul, et al. "Fully 3D printed 2.4 GHz bluetooth/wi-Fi antenna." International Symposium on Microelectronics. Vol. 2013. No. 1. International Microelectronics Assembly and Packaging Society, 2013.
8. Deffenbaugh, Paul I., Danielle M. Stramel, and Kenneth H. Church. "Increasing the Reliability of 3D Printing a Wi-Fi Sensor Device." International Symposium on Microelectronics. Vol. 2016. No. 1. International Microelectronics Assembly and Packaging Society, 2016.
9. Adams, Jacob J., et al. "Conformal printing of electrically small antennas on three-dimensional surfaces." Advanced Materials23.11 (2011): 1335-1340.
10. Paulsen, Jason A., et al. "Printing conformal electronics on 3D structures with Aerosol Jet technology." Future of Instrumentation International Workshop (FIIW), 2012. IEEE, 2012.
11. Hull, Charles W. "Apparatus for production of three-dimensional objects by stereolithography." U.S. Patent No. 4,575,330. 11 Mar. 1986.
12. Joe Lopes, Amit, Eric MacDonald, and Ryan B. Wicker. "Integrating stereolithography and direct print technologies for 3D structural electronics fabrication." Rapid Prototyping Journal 18.2 (2012): 129-143.
13. Cumpston, Brian H., et al. "Two-photon polymerization initiators for three-dimensional optical data storage and microfabrication." Nature 398.6722 (1999): 51.
14. Digaum, Jennefir L., et al. "Tight control of light beams in photonic crystals with spatially-variant lattice orientation." Optics express 22.21 (2014): 25788-25804.
15. Deckard, Carl R. "Method and apparatus for producing parts by selective sintering." U.S. Patent No. 4,863,538. 5 Sep. 1989.
16. https://www.ge.com/reports/ge-building-worlds-largest-additive-machine-3d-printing-metals/
17. http://optics.org/news/8/6/34
18. http://optics.org/news/8/9/25
19. MacDonald, Eric, and Ryan Wicker. "Multiprocess 3D printing for increasing component functionality." Science 353.6307 (2016): aaf2093.
20. Saleh, Ehab, et al. "3D inkjet printing of electronics using UV conversion." Advanced Materials Technologies 2.10 (2017).
21. Nassar, Ibrahim T., and Thomas M. Weller. "An electrically-small, 3-D cube antenna fabricated with additive manufacturing." Power Amplifiers for Wireless and Radio Applications (PAWR), 2013 IEEE Topical Conference on. IEEE, 2013.

22. Arnal, Nicholas, et al. "3D multi-layer additive manufacturing of a 2.45 GHz RF front end." Microwave Symposium (IMS), 2015 IEEE MTT-S International. IEEE, 2015.
23. Ketterl, Thomas P., et al. "A 2.45 GHz phased array antenna unit cell fabricated using 3-D multi-layer direct digital manufacturing." IEEE Transactions on Microwave Theory and Techniques 63.12 (2015): 4382-4394.
24. Flowers, Patrick F., et al. "3D printing electronic components and circuits with conductive thermoplastic filament." Additive Manufacturing 18 (2017): 156-163.
25. Wu, Sung-Yueh, et al. "3D-printed microelectronics for integrated circuitry and passive wireless sensors." Microsystems & Nanoengineering 1 (2015): 15013.
26. Kim, Chiyen, et al. "3D Printed Electronics With High Performance, Multi-Layered Electrical Interconnect." IEEE Access 5 (2017): 25286-25294.
27. Bailey, Callum, et al. "Augmenting Computer-Aided Design Software With Multi-Functional Capabilities to Automate Multi-Process Additive Manufacturing." IEEE Access 6 (2018): 1985-1994.
28. Carranza, Gilbert T., et al. "Design and Hybrid Additive Manufacturing of 3D/Volumetric Electrical Circuits." IEEE Transactions on Components, Packaging and Manufacturing Technology (2019).
29. Ubaldo Robles, Andelle Kudzal, and Raymond C. Rumpf, "Automated Hybrid 3D Printing of 3D Meandering Interconnects," IEEE Trans. on Components, Packaging, and Manufacturing Technology, 2019.
30. Li, J., et al. "Hybrid additive manufacturing of 3D electronic systems." Journal of Micromechanics and Microengineering 26.10 (2016): 105005.
31. Mirotznik, Mark S., et al. "Multi-material additive manufacturing of antennas." 2016 International Workshop on Antenna Technology (iWAT). IEEE, 2016.
32. B. A. Munk, "General Overview," in Frequency Selective Surfaces: Theory and Design, 1st ed, New York, New York, United States, Wiley, 2000, pp 1-25.
33. M. Harnois et al., "An Improved Fabrication Technique for the 3-D Frequency Selective Surface based on Water Transfer Printing Technology," Scientific reports, vol. 10, no. 1714, pp. 1-8, Oct. 2020.
34. T. Wu, "Four-band frequency selective surface with double-square-loop patch elements," IEEE Transactions on Antennas and Propagation, vol. 42, no. 12, pp. 1659-1663, Dec. 1994.
35. M. Mahmoodi and K. M. Donnell, "Novel FSS-based sensor for concurrent temperature and strain sensing," in IEEE International Symposium on Antennas and Propagation & USNC/URSI National Radio Science Meeting, San Diego, CA, USA, 2017, pp 679-680.
36. B. Munk, "Periodic surface for large scan angles," U.S. Patent No. 3,789,404, Jan. 29, 1974.
37. K. Sarabandi and N. Behdad, "A Frequency Selective Surface With Miniaturized Elements," IEEE Transactions on Antennas and Propagation, vol. 55, no. 5, pp. 1239-1245, May 2007.
38. P. Gurrala et al., "Fully Conformal Square-Patch Frequency-Selective Surface Toward Wearable Electromagnetic Shielding," IEEE Antennas and Wireless Propagation Letters, vol. 16, pp. 2602-2605, Aug. 2017.
39. R. Mittra, R. Hall, and Chich-Hsing Tsao, "Spectral-domain analysis of circular patch frequency selective surfaces," IEEE Transactions on Antennas and Propagation, vol. 32, no. 5, pp. 533-536, May 1984.
40. M. Fallah and M. H. Vadjed-Samieim, "Designing a Bandpass Frequency Selective Surface Based on an Analytical Approach Using Hexagonal Patch-Strip Unit Cell,"

Electromagnetics, vol. 35, no. 1, pp. 25-39, Dec. 2014. DOI: 10.1080/02726343.2015.971662.
41. J. Romeu and Y. Rahmat-Samii, “Fractal FSS: a novel dual-band frequency selective surface,” IEEE Transactions on Antennas and Propagation, vol. 48, no. 7, pp. 1097-1105, Jul. 2000.
42. J. P. Gianvittorio, Y. Rahmat-Samii, and J. Romeu, “Fractal FSS: various self-similar geometries used for dual-band and dual-polarized FSS,” in IEEE Antennas and Propagation Society International Symposium, Boston, MA, USA, 2001, pp. 640-643.
43. R. Mishra and R. Panwar, “Investigation of graphene fractal frequency selective surface loaded terahertz absorber,” Optical and Quantum Electronics, vol. 52, no. 317, pp.1-13, Jun. 2020. DOI: 10.1007/s11082-020-02433-2.
44. D. Z. Zhu, P. L. Wener, and D. H. Wener, “Design and Optimization of 3-D Frequency-Selective Surfaces Based on a Multiobjective Lazy Ant Colony Optimization Algorithm,” IEEE Transactions on Antennas and Propagation, vol. 65, no. 12, pp. 7137-7149, Oct. 2017.
45. J. Zhang et al., “A Novel 3D Ultra-wide Stopband Frequency Selective Surface for 5G Electromagnetic Shielding,” in 2020 International Symposium on Electromagnetic Compatibility-EMC EUROPE, Rome, Italy, 2020, pp. 1-4.
46. B. Liang et al., “Cylindrical Slot FSS Configuration for Beam-Switching Applications,” IEEE Transactions on Antennas and Propagation, vol. 63, no. 1, pp. 166-173, Nov. 2014.
47. C. Gu et al., “Dual-Band Electronically Beam-Switched Antenna Using Slot Active Frequency Selective Surface,” IEEE Transactions on Antennas and Propagation, vol. 65, no. 3, pp. 1393-1398, Jan. 2017.
48. R. C. Rumpf et al., “Guided-Mode Resonance Filter Compensated to Operate on a Curved Surface,” Progress In Electromagnetics Research C, vol. 40, pp. 93-103, May 2013. DOI: 10.2528/PIERC13041209.
49. J. H. Barton et al., “All-Dielectric Frequency Selective Surfaces with Few Number of Periods,” Progress In Electromagnetics Research B, vol. 41, pp. 269-283, Jun. 2012. DOI: 10.2528/PIERB12042404.
50. J. H. Barton et al., “3-D Printed All-Dielectric Frequency Selective Surface With Large Bandwidth and Field of View,” IEEE Transactions on Antennas and Propagation, vol. 63, no. 3, pp. 1032-1039, Jan. 2015.
51. H. A. Wheeler, “Simple relations derived fom a phased-array antenna made of an infinite current sheet,” IEEE Transactions on Antennas and Propagation, vol. 13, no. 4, pp. 506-514, Jul. 1965.
52. B. Munk et al., “A low-profile broadband phased array antenna,” in IEEE Antennas and Propagation Society International Symposium. Digest. Held in conjunction with: USNC/CNC/URSI North American Radio Sci. Meeting (Cat. No. 03CH37450), Columbus, OH, USA, 2003, pp. 448-451.
53. S. Soltani et al., “Popup Tunable Frequency Selective Surfaces for Strain Sensing,” IEEE Sensors Letters, vol. 4, no. 4, pp 1-4, Mar. 2020. DOI: 10.1109/LSENS.2020.2983685
54. V. Krushna Kanth and S. Raghavan, “EM Design and Analysis of Frequency Selective Surface Based on Substrate-Integrated Waveguide Technology for Airborne Radome Application,” IEEE Transactions on Microwave Theory and Techniques, vol. 67, no. 5, pp. 1727-1739, Apr. 2019.

55. X. Cuilian et al., “A novel dual-stop-band FSS for infrared stealth application,” in 2017 International Applied Computational Electromagnetics Society Symposium (ACES), Suzhou, China, 2017, pp. 1-2.
56. C. Sudhendra et al., “Design and implementation of a novel rasorber for aircraft stealth applications,” in 2014 First International Conference on Computational Systems and Communications (ICCSC), Trivandrum, India, 2014, pp. 176-180.
57. V. K. Varadan et al., “Conformal fractal antenna and FSS for low-RCS applications,” in SPIE's 7th Annual International Symposium on Smart Structures and Materials, Newport Beach, CA, USA, 2000, pp. 138-145.
58. T. Tian et al., “ Flexible and Reconfigurable Frequency Selective Surface With Wide Angular Stability Fabricated With Additive Manufacturing Procedure,” IEEE Antennas and Wireless Propagation Letters, vol. 19, no. 12, pp. 2428-2432, Oct. 2020. DOI: 10.1109/LAWP.2020.3034944
59. R. A. Mellita, S. S. Karthikeyan, and P. Damodharan, “Additively Manufactured Conformal All-dielectric Frequency Selective Surface,” in 2020 50th European Microwave Conference (EuMC), Utrecht, Netherlands, 2021, pp. 772-775.
60. M. Wang et al., “Research and implementation of a non-supporting 3D printing method based on 5-axis dynamic slice algorithm,” Robotics and Computer-Integrated Manufacturing, vol. 57, pp. 496-505, Jun. 2019.
61. I. M. Ehrenberg, S. E. Sarma, and B. Wu, “Fully conformal FSS via rapid 3D prototyping,” in Proceedings of the 2012 IEEE International Symposium on Antennas and Propagation, Chicago, IL, USA, 2012, pp. 1-2.
62. N. Begam et al., “Design of compact patch type curved frequency selective surface,” International Journal of RF and Microwave Computer-Aided Engineering, vol. 29, no. 9, Apr. 2019.
63. N. Begam et al., “Design of curved frequency selective surface with high roll off,” Microwave and Optical Technology Letters, vol. 59, no. 10, pp. 2660-2664, Oct. 2017.
64. Y. Zhang et al., “Electromagnetic Analysis of a Jigsaw-Shaped FSS for Conformal Application,” in 2020 50th European Microwave Conference (EuMC), Utrecht, Netherlands, 2021, pp. 768-771.
65. H. Fernandez Alvarez et al., “3D conformal bandpass millimeter-wave frequency selective surface with improved fields of view,” Scientific Reports, vol. 11, no. 12846, pp. 1-12, May 2021.
66. C. Pelletti et al., “Analysis of Finite Conformal Frequency Selective Surfaces via the Characteristic Basis Function Method and Spectral Rotation Approaches,” IEEE Antennas and Wireless Propagation Letters, vol. 12, pp. 1404-1407, Oct. 2013. DOI: 10.1109/LAWP.2013.2287377
67. U. d’Elia et al., “A Physical Optics Approach to the Analysis of Large Frequency Selective Radomes,” Progress in Electromagnetics Research, vol. 138, pp. 537-553, Apr. 2013. DOI: 10.2528/PIER13012810
68. R. C. Rumpf and J. Pazos, “Synthesis of spatially variant lattices,” Optics Express, vol. 20, no. 14, pp. 15263-15274, Jun. 2012.
69. R. C. Rumpf et al., “Electromagnetic isolation of a microstrip by embedding in a spatially variant anisotropic metamaterial,” Progress in Electromagnetic Research, vol. 142, pp. 243-260, Sep. 2013.

70. C. Xia et al., “Cylindrical-lens-embedded photonic crystal based on self-collimation,” Optics Express, vol. 30, no. 6, pp. 9165-9180, Mar. 2022.
71. E. A. Berry and R. C. Rumpf, “Generating Spatially-Variant Metamaterial Lattices Designed from Spatial Transforms,” Progress In Electromagnetic Research M, vol. 92, pp. 103-113, May 2020.
72. T. Smith et al., “An FSS-Backed 20/30 GHz Circularly Polarized Reflectarray for a Shared Aperture L- and Ka-Band Satellite Communication Antenna,” IEEE Transactions on Antennas and Propagation, vol. 62, no. 2, pp. 661-668, Nov. 2013.
73. M. R. Chaharmir et al., “Dual-band Ka/X reflectarray with broadband loop elements,” IET Microwaves, Antennas & Propagation, vol. 4, no. 2, pp. 225-231, Feb. 2010.
74. G. Zheng et al., “Metasurface holograms reaching 80% efficiency,” Nature nanotechnology, vol. 10, no. 4, pp. 308-312, Feb. 2015.
75. D. Lin et al., “Dielectric gradient metasurface optical elements,” Science, vol. 345, no. 6194, pp. 298-302, Jul. 2014.
76. R. C. Rumpf et al., “Spatially variant periodic structures in electromagnetics,” Philosophical Transactions of the Royal Society A: Mathematical, Physical and Engineering Sciences, vol. 373, no. 2049, Feb. 2015.
77. Robles, Ubaldo Robles. Hybrid 3D Printing Demonstrated by Arbitrary 3D Meandering Transmission Lines. The University of Texas at El Paso, 2018.
78. Tsang, Harvey Hing-Cheong. Digital processes and characterization for fabricating 3D RF devices. The University of Texas at El Paso, 2016.
79. https://kraetonics.com/
80. M. Hosseini, A. Pirhadi, and M. Hakkak, “A Novel AMC with Little Sensitivity to the Angle of Incidence Using 2-Layer Jerusalem Cross FSS,” Progress In Electromagnetics Research, vol. 64, pp. 43-51, Aug. 2006. DOI: 10.2528/PIER06061301.
81. Hsing-Yi Chen et al., “Bandwidth enhancement using dual-band frequency selective surface with Jerusalem cross elements for 2.4/5.8 GHz WLAN antennas,” in 2010 IEEE International Conference on Wireless Information Technology and Systems, Honolulu, HI, USA, 2010, pp. 1-4.
82. I. Sohail et al., “A linear to circular polarization converter based on Jerusalem-Cross frequency selective surface,” in 2013 7th European Conference on Antennas and Propagation (EuCAP), Gothenburg, Sweden, 2013, pp. 2141-2143.
83. Chu, Lan Jen. "Physical limitations of omni-directional antennas." Journal of applied physics 19.12 (1948): 1163-1175.
84. McLean, James S. "A re-examination of the fundamental limits on the radiation Q of electrically small antennas." IEEE Transactions on antennas and propagation 44.5 (1996): 672.
85. Grimes, Dale M., and Craig A. Grimes. "Radiation Q of dipole-generated fields." Radio Science 34.2 (1999): 281-296.
86. Davis, W. A., et al. "Fundamental limits on antenna size: a new limit." IET microwaves, antennas & propagation 5.11 (2011): 1297-1302.
87. Yang, Tae-Young. Fundamental limits on antenna size for frequency and time domain applications. Diss. Virginia Polytechnic Institute and State University, 2012.
88. Yang, Taeyoung, William A. Davis, and Warren L. Stutzman. "The design of ultra-wideband antennas with performance close to the fundamental limit." Proc. URSI General Assembly. 2008.

89. Best, Steven R. "The radiation properties of electrically small folded spherical helix antennas." IEEE Transactions on antennas and propagation 52.4 (2004): 953-960.
90. Clark, Jeffrey, and Abroad Safaai-Jazi. "Multifilar hemispherical helical antennas." IEEE Antennas and Propagation Society Symposium, 2004.. Vol. 3. IEEE, 2004.
91. Paulsen, Lee, et al. "Recent investigations on the volcano smoke antenna." IEEE Antennas and Propagation Society International Symposium. Digest. Held in conjunction with: USNC/CNC/URSI North American Radio Sci. Meeting (Cat. No. 03CH37450). Vol. 3. IEEE, 2003.
92. Patel, S. S., I. J. Garcia Zuazola, and W. G. Whittow. "Antenna with three dimensional 3D printed substrates." Microwave and Optical Technology Letters 58.4 (2016): 741-744.
93. Lomakin, K., et al. "3d printed helix antenna for 77ghz." 2020 14th European Conference on Antennas and Propagation (EuCAP). IEEE, 2020.
94. Lopez, Aida Garcia, Rohit Chandra, and Anders J. Johansson. "Optimization and fabrication by 3D printing of a volcano smoke antenna for UWB applications." 2013 7th European Conference on Antennas and Propagation (EuCAP). IEEE, 2013.
95. Liang, Fengchao, and Jinsong Gao. "A novel method for fabricating curved frequency selective surface via 3D printing technology." International Symposium on Optoelectronic Technology and Application 2014: Laser Materials Processing; and Micro/Nano Technologies. Vol. 9295. SPIE, 2014.
96. Carranza, Valle, and Rumpf. “Hybrid Conformal Printing on Arbitrary Curved Surfaces via Three axis for Electronic and RF Applications,” in progress for submission to Additive Manufacturing.
97. Hess, Roland. Blender Foundations: The Essential Guide to Learning Blender 2.5. Routledge, 2013.
98. Villanueva, Nova. "UV Mapping." Beginning 3D Game Assets Development Pipeline. Apress, Berkeley, CA, 2022. 117-149.
99. Bridson, Robert. "Fast Poisson disk sampling in arbitrary dimensions." SIGGRAPH sketches 10.1 (2007): 1.
100. Ying, Xiang, et al. "An intrinsic algorithm for parallel poisson disk sampling on arbitrary surfaces." IEEE transactions on visualization and computer graphics 19.9 (2013): 1425-1437.

Vita

Cesar Luis Valle is a graduate student at the University of Texas at El Paso (UTEP). He has received both his bachelor's and master's degree in Electrical and Computer Engineering at UTEP in 2014 and 2016 respectively. He has performed his research at the EM Lab in a combination of computational electromagnetics and hybrid 3D printing. Currently he is an intern at Sandia National Labs.

His research topics have ranged from photonic crystals, 3D radio frequency (RF) interconnects, 3D/volumetric circuits, 3D/volumetric antennas, frequency selective surfaces (FSSs), and metamaterials. He was part of the team that developed the world's first true 3D/volumetric circuit. He holds 2 United States Patents for technologies in photonic crystals and in 3D/volumetric hybrid printing processes. He currently has another patent application pending on conformal frequency selective surfaces. A few of the journals his works have been featured on include Progress in Electromagnetics Research (PIER), IEEE Transactions on Components, Packaging, and Manufacturing Technology, IEEE Transactions on Antennas and Propagation, among others.

Contact Information: vallecesarluis@gmail.com